

ABSTRACT

ZADDACH, ALEXANDER JOSEPH. Physical Properties of NiFeCrCo-based High-Entropy Alloys. (Under the direction of Dr. Carl C. Koch).

Conventional alloy design has been based on improving the properties of a single base, or solvent, element through relatively small additions of other elements. More recently, research has been conducted on alloys that contain multiple principal elements, particularly multi-component equiatomic alloys. When such alloys form solid solution phases, they are termed “high-entropy alloys” (HEAs) due to their high configurational entropy. These alloys often have favorable properties compared to conventional dilute solution alloys, but their compositional complexity and relative novelty means that they remain difficult to design and their basic properties are often unknown.

The motivation for this work is a detailed experimental exploration of some of the basic physical properties of NiFeCrCo-based alloys. NiFeCrCoMn was one of the first equiatomic HEAs developed. As the compositional space within this single system is extremely large, this work focuses primarily on equiatomic alloys and a limited subset of non-equiatomic alloys chosen for their specific properties.

Several alloys are prepared using both conventional methods (arc melting) and non-equilibrium methods (mechanical alloying). Properties studied include stacking fault energy, bulk mechanical properties, single crystal elastic constants, and magnetic properties.

The equiatomic NiFeCrCo and NiFeCrCoMn alloys were found to have a moderate to low stacking fault energy, $18 - 30 \text{ mJ m}^{-2}$. As they are single-phase, fcc alloys, they have high tensile ductility. Additionally, they also exhibit high work-hardening rates, resulting in high toughness. NiFeCrCo outperforms the 5-component equiatomic alloy in ductility and toughness. A 5-component alloy with higher Co content to reduce the stacking fault energy

also performs well. The single crystal elastic constants were measured using nanoindentation modulus measurements of grains of known orientation. The measured elastic constants were consistent with those calculated using first-principles modeling. Adding Zn in addition to Mn resulted in an alloy that preferred to form multiple phases. After the optimal heat treatment, it forms nano-sized grains of FeCo, which results in permanent magnetic behavior at room temperature.

© Copyright 2015 by Alexander J. Zaddach

All Rights Reserved

Physical Properties of NiFeCrCo-based High-Entropy Alloys

by
Alexander Joseph Zaddach

A dissertation submitted to the Graduate Faculty of
North Carolina State University
in partial fulfillment of the
requirements for the degree of
Doctor of Philosophy

Materials Science and Engineering

Raleigh, North Carolina
2015

APPROVED BY:

Dr. Carl Koch
Committee Chair

Dr. Ronald Scattergood

Dr. Douglas Irving

Dr. Yuntian Zhu

BIOGRAPHY

Alexander was born in Dearborn, Michigan to parents Alexis and Randy in June 1989. He attended Gabriel Richard High School in Riverview, Michigan, graduating in 2007. He then continued his education at Case Western Reserve University as a Materials Science and Engineering major and Economics minor, graduating with a Bachelor of Science in Engineering degree in 2011. While at CWRU, he conducted research on metallic glasses and nickel superalloys with Dr. John Lewandowski. He also worked at Powdermet Inc., in Euclid, Ohio from 2010 to 2011, which helped to develop his interest in powder metallurgy and non-equilibrium processing. He enrolled in the Materials Science and Engineering doctorate program at North Carolina State University in August 2011. There, under the direction of Dr. Carl Koch and in collaboration with Dr. Douglas Irving, he researched the properties of multi-component “high-entropy” alloys.

ACKNOWLEDGMENTS

There are many people I must thank for their assistance throughout my graduate program.

First, I would like to thank Dr. Koch for his great supervision, ideas, and review throughout this work.

Next, I would like to thank the faculty of the Materials Science and Engineering department, especially my other committee members, Dr. Scattergood, Dr. Irving, and Dr. Zhu. I would also like to thank many of the other students and postdoctoral researchers in the department that I worked closely with throughout my time at NCSU, particularly Changning Niu for his excellent computational work, Min Fan for his help with magnetic measurements and sample prep, Adedapo Oni for TEM analysis of my samples, and Jacob Majikes for help with the nanoindenter. I would also like to thank the scientists at the Analytical Instrumentation Facility, particularly Charles Mooney and Roberto Garcia for their expert training and advice. Additionally, I would like to thank Edna Deas, who has helped to navigate me through the often-complex processes within the university.

I would also like to thank my family, who has provided constant support and encouragement throughout my entire education. I have been fortunate to have such amazing support.

Finally, I also acknowledge support from the National Science Foundation from the Metals and Metallic Nanostructures program under grant DMR-1104930.

TABLE OF CONTENTS

LIST OF TABLES	x
LIST OF FIGURES	xi
1. INTRODUCTION	1
2. LITERATURE REVIEW	4
2.1. Multi-principal element/high-entropy alloys	4
2.1.1. Alloy design guidelines	6
2.2. NiFeCrCo alloys	9
2.3. Strengthening mechanisms in HEAs	11
2.3.1 Grain boundary strengthening	11
2.3.2. Stacking fault energy and strain-hardening	12
2.3.3. Solid solution strengthening	13
3. EXPERIMENTAL METHODS	15
3.1. Alloy synthesis	15
3.1.1. High-energy ball milling/mechanical alloying	15
3.1.1. Arc melting/casting	16
3.2. Thermal and mechanical processing treatments	17
3.2.1. Cold rolling	17
3.2.2. Annealing	17
3.2.3. Recrystallization	18
3.3. Mechanical testing	19
3.3.1. Microhardness	19
3.3.2. Tensile testing	20
3.3.3. Nanoindentation	22
3.4. Microstructure characterization	22
3.3.1. X-ray diffraction	22
3.3.2. Optical microscopy	25
3.3.3. Electron microscopy	25
3.5. Magnetic testing	27
4. MECHANICAL PROPERTIES AND STACKING FAULT ENERGIES OF NiFeCrCoMn HIGH ENTROPY ALLOY	28

4.1. Abstract	28
4.2. Introduction	29
4.3. Methods	33
4.3.1. Experimental	33
4.3.2. Computational	36
4.4. Results and discussion	40
4.4.1 X-ray diffraction	40
4.4.2 Single crystal elastic constants	42
4.4.3 Polycrystalline elastic constants	45
4.4.4. Stacking fault energy	47
4.4.5. Mechanical properties	52
4.5. Summary	53
5. TENSILE PROPERTIES OF LOW STACKING FAULT ENERGY HIGH ENTROPY ALLOYS	55
5.1. Abstract	55
5.2. Introduction	56
5.3. Experimental procedure	58
5.4. Results and discussion	60
5.4.1. Recrystallization and grain growth behavior	60
5.4.2. Tensile tests	62
5.4.3. Strain-hardening behavior	73
5.4.4. Effect of stacking fault energy	79
5.5. Conclusion	80
6. SINGLE CRYSTAL ELASTIC CONSTANTS OF EQUIATOMIC NiFeCrCoMn DETERMINED BY NANOINDENTATION	82
6.1. Abstract	82
6.2. Introduction	82
6.3. Experimental procedure	84
6.4. Results and discussion	86
6.5. Conclusions	89
7. STRUCTURE AND MAGNETIC PROPERTIES OF A MULTI- PRINCIPAL ELEMENT Ni-Fe-Cr-Co-Zn-Mn ALLOY	90

7.1. Abstract	90
7.2. Introduction	91
7.3. Methods	92
7.4. Results and discussion	94
7.4.1. Alloy structure	94
7.4.2. Magnetic properties	103
7.5. Conclusion	110
8. CONCLUSIONS	112
REFERENCES	115
APPENDIX	129
Code for calculation of elastic constants using nanoindentation data	130

LIST OF TABLES

Table 4.1. Atomic radii and valence electron concentration of pure metals [87].	32
Table 4.2. Composition, average VEC, and ideal entropy of mixing of alloys produced.	33
Table 4.3. SQS for NiFeCrCo and NiFeCrCoMn alloys containing 24 and 20 atoms, respectively. Initial atomic positions are in Cartesian coordinates scaled by the lattice parameter.	39
Table 4.4. Poisson's ratio of NiFeCrCo and NiFeCrCoMn from DFT calculations.	46
Table 4.5. Young's modulus of NiFeCrCo and NiFeCrCoMn from DFT calculations and experiment.	47
Table 4.6. SFEs of NiFeCrCo and NiFeCrCoMn calculated from experimental data of stacking fault probability and DFT calculations of elastic constants.	49
Table 4.7. SFE of non-equiatomic HEAs.	51
Table 4.8. Hardness and grain size measurements from the as-milled powders and cast alloys.	53
Table 5.1: Alloys used in the study, their stacking fault energies[18,123], enthalpy[33] and entropy of mixing, and RMS-deviation from average atomic size (δ)[3,39].	58
Table 5.2: Numerical results of tensile tests: yield stress, tensile stress, percent elongation, uniform elongation, and tensile toughness (calculated as the integral of the engineering stress-strain curve). Values for three TWIP steels are included for comparison[127].	67
Table 6.1: Measured indentation moduli, polycrystalline elastic properties, and single crystal elastic constants of NiFeCrCoMn.	88
Table 7.1: Phases identified in the 1 hour/500 °C sample, their lattice parameters (and estimated standard deviation), published lattice parameters from the PDF-4+ database [149], and composition.	98
Table 7.2: Close-packed atomic radii of the elements [39].	100
Table 7.3: Grain size statistics of precipitate phases in 1 hour/500 °C sample.	101

LIST OF FIGURES

Figure 3.1. Diagram of recrystallization process	19
Figure 3.2. Representative tensile specimen.....	20
Figure 4.1. XRD patterns of as-milled equiatomic NiFe, NiFeCr, NiFeCrCo, and NiFeCrCoMn.	41
Figure 4.2. Elastic constants of equiatomic NiFeCrCo (a) and NiFeCrCoMn (b) [46].....	44
Figure 4.3. Ratio of mean-square microstrain to stacking fault probability for NiFe, NiFeCr, NiFeCrCo, and NiFeCrCoMn. Error bars represent error from the stacking fault probability measurement.	48
Figure 4.4. SFEs of equiatomic fcc metals from pure Ni to NiFeCrCoMn [73,117].....	50
Figure 4.5. Ratio of mean-square microstrain to stacking fault probability for 5-component alloys. Error bars represent error from the stacking fault probability measurement. Circles represent alloys in which Cr balances the difference in Ni content. The triangle is the alloy in which the concentrations of all other elements are increased equally to balance the Ni.....	51
Figure 4.6. SFEs of equiatomic NiFeCrCoMn and $\text{Ni}_{14}\text{Fe}_{20}\text{Cr}_{26}\text{Co}_{20}\text{Mn}_{20}$ (“Best HEA”) compared to other low SFE alloys [57,116,118].	52
Figure 5.1: Hardness vs annealing temperature after ~80% rolling reduction (AR = as-rolled).....	61
Figure 5.2: Representative tensile stress-strain curves for (a) NiFeCrCo (625 °C and 1100 °C), (b) NiFeCrCoMn (650 °C and 1100 °C), (c) $\text{Ni}_{18.5}\text{Fe}_{18.5}\text{Cr}_{18.5}\text{Co}_{26}\text{Mn}_{18.5}$ (625 °C and 1100 °C), and (d) $\text{Ni}_{14}\text{Fe}_{20}\text{Cr}_{26}\text{Co}_{20}\text{Mn}_{20}$ (675 °C and 1100 °C). Red lines – moderate temperature anneal, black lines – high temperature anneal.	63
Figure 5.3: Secondary electron images of the fracture surfaces of (a) NiFeCrCo and (b) NiFeCrCoMn.....	70
Figure 5.4: Gage surfaces of $\text{Ni}_{18.5}\text{Fe}_{18.5}\text{Cr}_{18.5}\text{Co}_{26}\text{Mn}_{18.5}$ after testing. (a) Backscattered electron image of 1100 °C sample. (b) AFM image of 625 °C sample.	72
Figure 5.5: Strain-hardening rate (left axis) and exponent (right axis) as a function of true stress subtracted by yield stress for (a) NiFeCrCo, (b) NiFeCrCoMn, (c) $\text{Ni}_{18.5}\text{Fe}_{18.5}\text{Cr}_{18.5}\text{Co}_{26}\text{Mn}_{18.5}$, and (d) $\text{Ni}_{14}\text{Fe}_{20}\text{Cr}_{26}\text{Co}_{20}\text{Mn}_{20}$ (1100 °C only). Color key: Black: coarse-grain strain-hardening rate. Blue: coarse-grain exponent. Red: fine-grain rate. Green: fine-grain exponent.	75

Figure 6.1: EBSD map of NiFeCrCoMn. The reference pattern is visible as a white (unindexed) region near the center.....	85
Figure 6.2: Load vs. depth curve for {111} grain.....	86
Figure 7.1: XRD pattern of (a) as-milled NiFeCrCoZnMn alloy and (b) alloy after 1 hour, 500 °C anneal.	96
Figure 7.2: EDS maps showing the distribution and morphology of precipitate phases after 1 hour, 500 °C anneal.	97
Figure 7.3: Magnetization vs. field curve for 1 hour/500 °C sample	104
Figure 7.4: Magnetic properties as a function of annealing temperature and time. a) Saturation magnetization, b) intrinsic coercivity, c) remanence, and d) maximum energy product.	105

1. INTRODUCTION

Solid solution, equiatomic, multi-principal element alloys are a relatively recent development in the field of alloy design [1,2]. These are often called high-entropy alloys (HEAs) due to the high configurational entropy associated with a multi-component solid solution. They have attracted increasing attention as a potential new paradigm in alloy development [3]. Rather than attempting to improve the properties of a single pure metal through the addition of smaller amounts of other elements, HEAs essentially create entirely new alloy systems for materials scientists to develop. These systems can have much better properties than pure elemental metals. However, because of their complexity and relative novelty, there are still several major challenges that must be solved before they can be employed as engineering materials. Namely, alloy design rules for HEAs are not fully developed, they can be difficult to model, and many of their basic physical properties remain unknown.

The primary motivation for this work is to address this third challenge. By measuring the physical properties of the base alloy system and how they are affected by changes to the composition, the potential applications of the alloy system can be determined. The basic physical properties are also of use to engineers and scientists as data for model improvements, for development of processing methods, and for research into related properties.

The majority of the research regarding multi-principal element alloys has focused on single-phase alloys, which could be called “true” high-entropy alloys. However, multi-phase

alloys are of significant engineering interest and some research has shown that the actual importance of the high configurational entropy may have been overemphasized initially [4], so this work describes both types of alloys.

This work begins with an overview of the literature relating to multi-principal element alloys, the NiFeCrCo alloy system, and other topics relevant to the physical properties that were investigated. Next, a detailed description of the procedures and relevant theory of the experimental methods used is given. Each chapter describing results also contains a detailed introduction and full description of the experimental methods.

Chapter 4 contains a combined experimental and computational study of the mechanical properties and stacking fault energy of equiatomic alloys and some non-equiatomic 5-component alloys. The computationally determined elastic properties are combined with stacking fault probabilities measured using x-ray diffraction to determine the stacking fault energy of the alloys. The hardness of the various 5-component alloys is also measured.

Chapter 5 describes the results of tensile tests of NiFeCrCo, NiFeCrCoMn, and the non-equiatomic NiFeCrCoMn alloys determined in chapter 4 to have a low stacking fault energy. The recrystallization temperatures of the alloys are determined after cold rolling and tensile tests are conducted on both fine-grained and coarse-grained samples. The basic mechanical properties are calculated from the stress-strain curves and the strain-hardening behavior of the alloys is compared. The fracture surfaces of the samples is characterized to interpret the differences in ductility between the different alloys.

In chapter 6, the single crystal elastic constants of NiFeCrCoMn are experimentally measured using nanoindentation. The results are compared to the computationally determined constants in chapter 4 and the stacking fault energy is recalculated using the measured constants.

Finally, chapter 7 describes a NiFeCrCoMnZn alloy. The microstructure after mechanical alloying and various heat treatments is characterized using x-ray diffraction and electron microscopy. The magnetic properties are also measured and related to the microstructure. The experimental characterization is complemented by first-principles modeling of the alloy's phases.

2. LITERATURE REVIEW

2.1. Multi-principal element/high-entropy alloys

Conventional alloy development is primarily based on improving the properties of a single base or solvent element through additions of other elements to improve specific properties. Historically, this was used to produce simple binary alloys such as the addition of Zn to Cu to improve its mechanical properties or Cu to Ag to increase strength and mechanical properties. A similar paradigm is still used in modern alloys, such as the addition of Re to nickel-base superalloys to slow γ' coarsening[5] or the addition of Sc to stabilize nanocrystalline grains in steel [6]. In recent years, starting around 2004 [1,2], interest has grown in alloys with multiple principal elements that consist primarily of a single solid solution phase. These alloys have come to be called “high-entropy” alloys (HEAs), as it was originally hypothesized that the high configurational entropy, given for an equiatomic ideal solution as:

$$\Delta S_{conf} = R \ln n \quad (2.1)$$

where n is the number of components helps to stabilize the solid solution phase. As $\Delta G = \Delta H - T\Delta S$, a high configurational entropy will serve to reduce the free energy of the solid solution phase [2]. Some of the first examples of these alloys were NiFeCrCoMn, which forms a single fcc phase[1] and CuCoNiCrAl_xFe, which forms fcc, bcc, or mixed solid solutions depending on Al content [2]. Later, alloy systems based on refractory metals, such as VNbMoTaW were produced that form single phase bcc solid solutions [7]. hcp HEAs have been produced, but appear to occur much less frequently than fcc and bcc [8–11]. Most

HEAs have been produced by arc melting[12–14,3] or mechanical alloying [3,15–18], though some have also been produced as coatings or films using thermal spray[19], laser cladding[20], magnetron sputtering [21], and electrochemical methods [22]. The common definition of a HEA is an alloy with 5 or more elements with atomic fractions between 5 – 35 at% [2,23,24] or with a configurational entropy $\geq 1.61R$ ($13.39 \text{ J mol}^{-1} \text{ K}^{-1}$) [25]. Alloys with 2 – 4 principal components have been described as “medium entropy” alloys [24–26].

There are 28 non-radioactive transition metals, 6 commonly-used p-block metals, and 5 alkaline earth metals (excluding Ra). Using only 5-element equiatomic systems, this allows for 575,757 possible unique combinations ($n!/r!(n-r)!$). Later research however, showed that the high entropy hypothesis might not actually be applicable for most alloy systems. Otto et al. used the known single-phase NiFeCrCoMn alloy, replaced individual elements with another that had the same crystal structure and similar size or electronegativity, and subjected the alloys to an extended annealing treatment. Only the NiFeCrCoMn alloy was found to form a stable single solid solution. Other alloys phase-separated or formed intermetallic compounds. This was attributed to the enthalpy contribution to the free energy, which in many intermetallic systems is more significant than the configurational entropy of a random solid solution. As a result, this drastically reduces the number of possible combinations that will form a “true” HEA [27]. Further considerations will be discussed below. Of course, this is not to say that multiphase alloys are of no use. Many important engineering materials consist of multiple phases, which can produce properties unobtainable in only a solid solution. A multi-phase multi-principal element alloy with interesting magnetic properties

will be discussed in Chapter 7. Other multi-principal alloys have been developed with precipitation-hardening capabilities [28].

2.1.1. Alloy design guidelines

Developing HEAs has additional challenges beyond those of conventional alloy development. In particular, since most conventional alloys consist of a single solvent element, binary phase diagrams are often sufficient to predict equilibrium phases. As such, binary phase diagrams are often the only published diagrams for which data is available through the entire compositional range. Ternary phase diagrams are unavailable for many systems and may only include data for relatively dilute mixtures [1,3,29]. Previously it was generally assumed that such multi-component mixtures would be almost certain to form complex systems with multiple phases. For a c component system at constant pressure, the Gibbs phase rule predicts a maximum of $c + 1$ phases at equilibrium [1,29]. Additionally, glass formation is often aided by multiple components via the “confusion principle” [30]. Finally, computational modeling is also more difficult in multi-component systems due to the lack of data regarding concentrated multi-component mixtures [29,31] and the difficulty in modeling a random solution using a periodic cell [3,18,32].

In addition to the aforementioned challenges, the conventional substitutional solid-solution design guidelines – the Hume-Rothery rules – do not fully apply to HEAs. Solutions of elements with different crystal structures in their pure states can be formed and there is no meaningful distinction between solvent and solute elements when all are present in nearly

equal concentrations. Additionally, some HEAs contain elements with significantly different electronegativity [3]. Because of these shortcomings, other empirical rules have been proposed by several authors in an attempt to describe the phase formation behavior of alloys containing multiple principal elements.

The proposed rules for determining the likelihood of solid solution formation are based on thermodynamic and atomic size calculations for the alloy. The ideal mixing enthalpy can be calculated as [3]:

$$\Delta H_{mix} = \sum_{i=1, i \neq j}^N 4\Delta H_{AB}^{mix} c_i c_j \quad (2.2)$$

where ΔH_{AB}^{mix} is the enthalpy of mixing for the binary combination of elements A and B, typically given by Miedema's model [33–35]. Using this, the ideal mixing entropy (equation 2.1), and the average melting temperature of the elements in the alloy a unitless parameter, Ω , can be defined:

$$\Omega = \frac{T_m \Delta S_{mix}}{|\Delta H_{mix}|} \quad (2.3)$$

Empirical studies have shown that alloys must have an Ω of at least 1.1 in order to form solid solutions [3]. This alone is not a sufficient predictor of solid solution stability, however, so an additional criterion, δ , has been proposed to account for atomic size mismatch:

$$\delta = \sqrt{\sum_{i=1}^N c_i \left(1 - \frac{r_i}{\sum_{i=1}^N c_i r_i}\right)^2} \quad (2.4)$$

In empirical studies, alloys with $\delta \geq 6.6\%$ did not form solid solutions (primarily forming metallic glasses), while some alloys with $4\% < \delta < 6.6\%$ formed a mixture of solid solution and intermetallic phases, even when the Ω parameter is > 1.1 . Alloys with $\delta < 4\%$ are most likely to form solid solutions [3,36]. These rules are entirely empirical however, and somewhat limited. The thermodynamic guidelines assume ideal or regular solutions, while many, if not most, metallic solutions are not regular [37,38]. Additionally, the formation enthalpies of intermetallic compounds are typically more negative than the enthalpy of mixing for the same alloy [37]. In a sub-regular solution, the Gibbs free energy of mixing vs. composition curve is not symmetrical, thus the most stable solution may have a non-equiatomic composition [38]. Also, there are several methods used to calculate the atomic radii, depending on bond type and packing which can give significantly different results [39,40]. The metallic radius calculated with coordination number 12 is the most applicable to HEAs, as they have close-packed crystal structures [3,39,40].

Additionally, some attempts have been made to predict which solid solution phase will form in a given alloy. An empirical rule based on the average valence electron concentration (VEC) has been developed to predict fcc or bcc phase formation. The electron to atom (e/a) ratio has historically been used in the analysis of solid solution alloys [41]. However, e/a ratios for transition metals are not all well-defined, so the simpler VEC, which consists of the total number of electrons, including d-electrons, in the valence band, is used instead [42]. Alloys with a weighted-average $VEC \geq 8$ tend to form fcc phases, while alloys with $VEC < 6.87$ tend to form bcc phases. Between this range, alloys tend to form a mix of

phases [42]. VEC has also been used to predict the formation of σ -phase intermetallics in Cr and V-containing alloys. Alloys with $6.88 < \text{VEC} < 7.84$ containing Cr or V are prone to σ -phase formation [43].

2.2. NiFeCrCo alloys

The first NiFeCrCo alloy, and the most common one described in the literature is NiFeCrCoMn, first developed by Cantor et al. in 2004 [1]. The alloy was notable for forming a solid solution despite the complex composition compared to conventional alloys. The majority of research has focused on this alloy, but other NiFeCrCo-based alloys have also been developed using Ti, Mo, and Al [17,44–46].

The majority of prior research on the alloy system, as well as the majority of the research in this work, has focused on its mechanical properties. Both the strength and ductility of equiatomic NiFeCrCo and NiFeCrCoMn increase at cryogenic temperatures compared to room temperature [24]. This was attributed to a change in deformation mechanisms at low temperatures. At room temperature, dislocation glide is the primary deformation mechanism. At cryogenic temperatures, deformation twinning becomes the dominant mechanism [13]. The fracture toughness of the alloy is also high, with $K_{JIC} \sim 220$ MPa m^{-1/2} at temperatures from 77 – 293 K [47]. Wu et al. found that the strength of NiFeCrCoMn multicomponent alloy systems is not dependent on the number of elements. NiCrCo has a higher strength and uniform elongation than 4-component alloys. Alloys containing Cr were generally stronger than those without it [4].

Haglund et al. measured the polycrystalline elastic constants using resonant ultrasound spectroscopy and found that at 300 K, $E = 202$ GPa and $\nu = 0.265$ [48]. Huang et al. found that the lattice elasticity of NiFeCrCoMn as a function of temperature deviates significantly from the nearly-linear behavior seen in pure metals and conventional stainless steel alloys [26]. The shear stress required to induce incipient plasticity in the alloy is $1/10 - 1/15$ of the shear modulus and the activation energy for the onset of plasticity is 1.7 ± 0.3 eV. The activation volume is $34 \pm 7 \text{ \AA}^3$, suggesting heterogeneous, vacancy-mediated nucleation as the mechanism behind the onset of plasticity [49]. Equiatomic NiFeCrCoMn forms a brass-type rolling texture after cold rolling and develops a recrystallization texture similar to that of twinning-induced plasticity steels with a high fraction of annealing twins [50].

The NiFeCrCoMn system was also used to determine the importance of enthalpy and entropy on the phase formation in HEAs. Otto et al. took the equiatomic alloy and made substitutions for single elements using similar elements such as Cu for Ni and V for Cr. However, only the original NiFeCrCoMn formed a complete solid solution. All of the other alloys formed intermetallics or phase separated. This was due to the effect of the enthalpy of formation of the secondary phases overwhelming the higher mixing entropy of the solid solution [27].

Tsai et al. found that the diffusion coefficients of the individual alloying elements in NiFeCrCoMn were lower than in pure metals and conventional alloys [51]. Niu et al. found that due to “magnetic frustration,” the Cr in NiFeCrCo prefers to order into the lattice corner sites. As a result, cast alloys tend to form ordered nano-domains. They also found that the

alloy is ferromagnetic at low temperatures. Both the Curie temperature and magnetic moment depend on the ordering in the alloy, which can be affected by processing methods such as ball milling and cold rolling [52].

2.3. Strengthening mechanisms in HEAs

As HEAs are single-phase alloys, the available strengthening mechanisms are limited to grain boundary strengthening in fine-grained and nanocrystalline alloys, solid solution strengthening, and strain hardening.

2.3.1 Grain boundary strengthening

Grain boundary strengthening is also commonly referred to as Hall-Petch strengthening, as it is described by the Hall-Petch equation:

$$\sigma_y = \sigma_0 + k/\sqrt{d} \quad (2.5)$$

where σ_y is the yield stress, σ_0 is the stress required to initiate dislocation motion, more specifically, the flow stress of an undeformed single crystal in an orientation that would allow multiple slip to occur, k is a material-specific constant, and d is the grain diameter [53]. This effect results from the discontinuity of the crystal lattice at grain boundaries. As a result, the grain boundaries act as a barrier to dislocation motion. Dislocations pile up at the grain boundaries until the stress at the tip reaches a critical shear stress, given by:

$$\tau_c = \frac{\pi\tau_s^2 D}{4Gb} \quad (2.6)$$

where τ_s is the applied stress minus the friction stress to overcome resistance to dislocation motion, G is the shear modulus, and b is the Burgers vector [54].

While this relation predicts that strength will continue increasing as grain size decreases to infinitesimally small sizes, in practice the relation tends to break down for grain sizes on the order of 10 nm. Below 10 nm, the grains are too small to support the necessary dislocation pile-up. In some materials, an negative k is observed in some materials below a certain size, termed “inverse Hall-Petch” effect. Several mechanisms have been proposed to explain this behavior using models based on dislocations, diffusion, grain-boundary shearing, and treating the grain boundary regions as a second phase [55].

2.3.2. Stacking fault energy and strain-hardening

Strain hardening, or work hardening, occurs when dislocations created by deformation pile up and obstruct further movement of dislocations. This can occur as a result of interactions between dislocation stress fields, interactions that lock dislocations, and the formation of jogs in the dislocation line. The effect of strain hardening on a stress-strain curve is commonly described by a power-law equation like:

$$\sigma = K\varepsilon^n \quad (2.7)$$

where σ and ε are true stress and strain, respectively, K is termed the strength coefficient, and n is the strain hardening exponent. $n=0$ indicates no strain hardening (a perfectly plastic material). Most metals are in the range $0.1 < n < 0.5$ [54].

The stacking fault energy (SFE) of an alloy can affect the strain hardening behavior. High SFE materials deform by dislocation glide and generally have lower strain hardening exponents [56]. In metals with low SFE, dislocations are more likely to dissociate into partial dislocations and the spacing between the partial dislocations (the stacking fault) increases with lower SFE. As a result, cross-slip and climb becomes more difficult, making it more likely that dislocations will be locked [54,57,58]. Low SFE materials are also more likely to deform by twinning. The deformation twins also act similarly to grain boundaries, increasing strength through a “dynamic Hall-Petch” process [13,59].

Reducing the SFE has been a promising method of producing new alloys with high strength and good ductility. Low-SFE metals also tend to exhibit a higher dislocation storage capacity, which, combined with deformation by twinning, increases ductility, while simultaneously increasing strength, resulting in a material with high toughness. In conventional alloys, this has been exploited to create “twinning induced plasticity” (TWIP) steels [59,60]. It has also been used to improve the ductility of ultrafine grained (UFG) and nanocrystalline (NC) materials, which are normally extremely strong, but brittle [61].

2.3.3. Solid solution strengthening

As high entropy alloys contain a high concentration of several elements, solid solution strengthening likely represents a significant contribution to the overall strength. Several factors affect solid solution strengthening behavior in metals. Size misfit of the atoms in solution can result in an elastic stress field around the misfitting atoms. If there is a

difference in modulus between the atoms in solution, this can result in a local change of the modulus of the crystal, which also creates a similar interaction to the size misfit [54,62]. Other strengthening effects can result from electrical interactions due to differing valences with the electrical dipoles of dislocations [54].

Ordering behavior in solid solutions can also affect the strength. The movement of a dislocation through a region of short-range order or solute clustering reduces the amount of local order, resulting in an energy increase and extra work required to continue moving the dislocation. In alloys that form superlattices, dislocations create anti-phase boundaries [54]. In alloys containing stacking faults, solute atoms may segregate to the faults if they have a preferential solubility in the hcp phase of the alloy. This lowers the effective stacking fault energy and increases the separation of the partial dislocations [54,63].

3. EXPERIMENTAL METHODS

3.1. Alloy synthesis

3.1.1. High-energy ball milling/mechanical alloying

To prepare samples by mechanical alloying, pure (>99%) elemental powders were weighed and loaded into stainless steel or tool steel vials in a high purity argon atmosphere. A ball to powder weight ratio of 10:1 was used with stainless steel balls.

In the mechanical alloying process, powder particles are repeatedly flatted, fractured, and cold-welded together from collisions between the media and particles [64]. NiFe and NiFeCr alloys were produced by cryogenic milling, using a SPEX 8000 mixer mill modified to chill the outside of the vial with liquid nitrogen. The low temperature reduces the ductility of the metal powders, preventing excessive cold welding of the powder to the milling media. NiFeCrCo and NiFeCrCoMn alloys were milled at room temperature in a standard SPEX 8000 mill with forced air cooling, with 2 drops (approximately 0.7 wt%) of dodecane added as a process control agent (PCA). PCAs adsorb onto the surface, inhibiting cold welding [64]. Dodecane was chosen due to the small amount needed to achieve the desired effect as well as for safety purposes – its flash point is 71 °C, meaning it does not easily combust in ambient conditions.

During the milling process, the particle size of the powder changes, but reaches an equilibrium point as the material work hardens and a balance is reached between cold welding and fracturing [64]. As the primary goal of this project was to produce alloys, the milling time was determined based on the necessary time to achieve complete alloying. This

varied from as short as 4 hours with binary NiFe alloys to more than 24 hours with some NiFeCrCoMn alloys. Complete alloying could be verified using x-ray diffraction and electron microscopy, described later in this chapter.

Mechanical alloying can result in contamination from the milling media itself. Since steel vials and balls were used, the primary contaminant was iron. Additionally, preferential cold welding of particular elements to the milling media can cause the composition of the alloy to differ slightly from the intended composition, despite precise measurement of the starting powders. When possible, this was corrected for, such as by reducing the amount of iron powder added. Because the mechanical alloying process affects the crystal structure, extended milling times can result in amorphization of the material[64], considered undesirable in this work. As a result, attempting to correct the composition after milling by adding more elemental powders and milling again is generally not possible.

3.1.1. Arc melting/casting

Bulk samples were prepared by arc melting and casting using equipment and a process similar to that described in [65]. Pure (>99%) elemental pieces are placed on a water-cooled copper hearth. A gas tungsten arc welding (GTAW) power supply and 98% W + 2% La₂O₃ electrode are used to generate an electric arc to heat and melt the materials. The entire process takes place inside of a sealed chamber that is evacuated to < 50 mTorr and refilled with high purity argon at least 3 times before operation. Before melting the sample, a small piece of pure titanium is heated to combine with any remaining oxygen in the chamber.

Because the bottom of the sample does not completely melt, the sample is flipped and remelted at least three times. Once well-mixed, the hearth is rotated slightly so that when melted, the molten metal drops into a water-cooled 7 mm diameter cylindrical copper mold. Samples for further processing and analysis were then cut from the cast cylinder using a low-speed diamond wafering saw. If chemical analysis revealed the actual composition deviated from the intended composition, additional pure elements could be added and the melting/casting process repeated.

3.2. Thermal and mechanical processing treatments

3.2.1. Cold rolling

In order to produce sheets of material that could be cut into tensile test samples, the cast samples were cold rolled after a homogenization heat treatment (described below). Multiple room temperature rolling passes were used to reduce the thickness of the samples to $< 500 \mu\text{m}$, resulting in an approximately 80% rolling reduction. As cold rolling results in a highly textured microstructure with grains elongated in the rolling direction and a high dislocation density, samples were recrystallized before testing.

3.2.2. Annealing

Powders and bulk samples were annealed in a quartz tube furnace in a 98% Ar + 2% H₂ atmosphere to prevent oxidation. The tube was fixed in position and the furnace was mounted on a track so that it could be moved over the tube. The tube was evacuated to < 50

mTorr and refilled with the Ar H₂ mixture at least three times before being moved into the furnace. Temperatures were measured using a type K (chromel/alumel) thermocouple inside the tube near the sample. Samples were placed in ceramic (typically alumina) boats to avoid direct contact with the sides of the tube. With the exception of the homogenization treatments, samples were cooled by removing the tube from the furnace immediately after the necessary time had elapsed. This allowed for fast cooling in ambient temperature but maintained the controlled atmosphere. Annealing times and temperatures varied depending on the sample and purpose.

Cast samples were homogenized at 1000 °C for 24 hours. For cooling, the furnace was switched off and the tube left inside, resulting in a slower cooling rate. This process reduces any micro-segregation from the casting process and results in an equiaxed grain structure.

3.2.3. Recrystallization

When sufficiently heated, metals that have been deformed undergo processes of recovery and recrystallization. In the recovery process, dislocations rearrange into lower-energy configurations, such as low-angle subgrain boundaries. In recrystallization, new strain-free grains form in place of the deformed microstructure. If the high temperature is maintained beyond the time necessary for recrystallization, the grains will coarsen in order to reduce the grain boundary area, a region of higher energy. Recrystallization is thermally activated, requiring some critical temperature to initiate the process. After nucleation, the

grains grow at a nearly constant rate until they begin to impinge on each other [66]. This process is illustrated in Figure 3.1 The recrystallization temperature is commonly defined as the temperature needed to achieve complete recrystallization in 1 hour [67], though the temperature needed for a given material will vary depending on the degree of deformation.

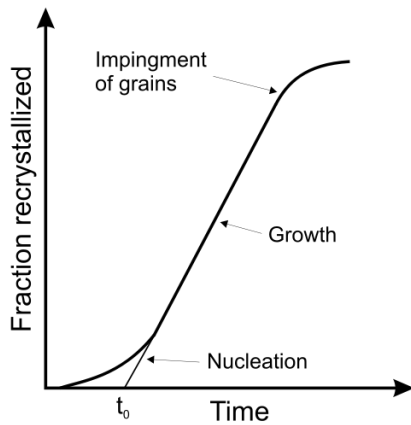


Figure 3.1. Diagram of recrystallization process

The recrystallization temperatures and grain coarsening behavior of alloys in this work was determined by annealing cold-rolled samples for 1 hour at temperatures from 575 – 1100 °C, then measuring the hardness as described below. As the strain-free recrystallized grains have a much lower strength than the work-hardened material, the hardness will drop substantially after recrystallization.

3.3. Mechanical testing

3.3.1. Microhardness

Microhardness tests were conducted with a Buehler microhardness tester with a Vickers indenter. Powder samples were fixed to a glass slide using a cyanoacrylate adhesive and polished using SiC papers. Bulk and compacted samples were also polished using SiC papers. At least 10 measurements were taken on each sample.

3.3.2. Tensile testing

After casting, homogenization, cold rolling, and recrystallization as described above, tensile test specimens were cut from the resulting sheet. The samples were cut using a miniature CNC milling machine and had a gage width of approximately 1 mm and gage length of 2.5 mm. The actual width and length of each sample was measured using optical microscopy and a calibrated microscope slide. After cutting, both sides of the sample were polished using SiC papers. A representative sample is shown below in Figure 3.2.

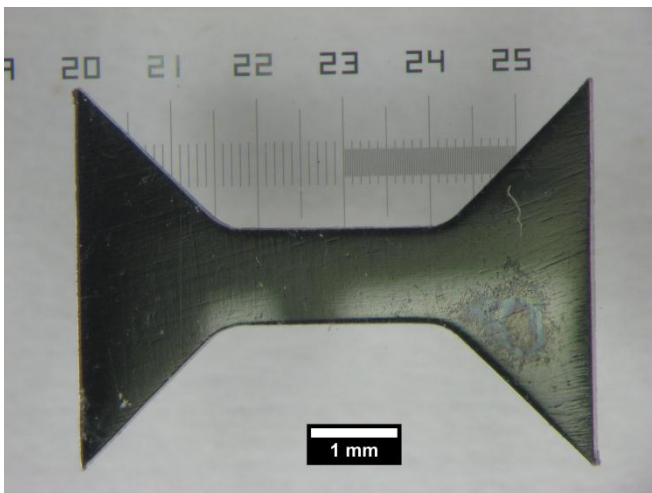


Figure 3.2. Representative tensile specimen

The samples were tested using a horizontally-mounted micro-tensile tester with grips designed to hold the shoulders of the samples. A 100 lb capacity load cell measured the applied force and a linear variable displacement transducer (LVDT) measured the total displacement. The raw voltage data from the load cell and LVDT was recorded using a National Instruments data acquisition device connected to a computer running the Igor Pro software. Tests were conducted at a strain rate of $7.3 \times 10^{-4} \text{ s}^{-1}$.

An Excel spreadsheet was used to convert the data from voltage to displacement and force, using formulas derived from tests of calibration materials and tests with no load. Using the previously measured thickness and width, the spreadsheet also calculates the engineering stress and using the measured starting length it calculates the engineering strain after applying a correction for machine deformation. Further analysis was done using Origin 9.5 and other Excel spreadsheets, including one to smooth the data using an adjacent-averaging method so that a numerical derivative could be found.

Several parameters are extracted from the resulting engineering stress-strain curve. The yield stress was determined using the 0.2% offset method, drawing a line parallel to the linear elastic portion, offset in the x direction by 0.002, and finding the intersection with the data. The ultimate tensile stress is the maximum stress value. The total percent elongation is the strain value at which failure occurred. The uniform elongation is the strain value at the ultimate tensile stress, the point at which necking begins. The toughness was estimated as the area under the curve, using the numerical integration feature of Origin [54,67].

Strain-hardening properties were derived from the true stress-strain curve. The conversion between engineering stress and true stress is given by [67]:

$$\sigma_T = \sigma_E(1 + \epsilon_E) \quad (3.1)$$

and the conversion between engineering strain and true strain is [67]:

$$\epsilon_T = \ln(1 + \epsilon_E) \quad (3.2)$$

The strain hardening rate can then be calculated as the derivative of the true stress-strain curve, from the yield point to the onset of necking. Additionally, the strain-hardening exponent, n , can be calculated [54]:

$$\frac{d\sigma}{d\epsilon} = n \frac{\sigma}{\epsilon} \quad (3.3)$$

3.3.3. Nanoindentation

Nanoindentation tests were done using a Hysitron Triboindenter with a 100 nm radius Berkovich tip. The area function was calibrated by indenting a sample of fused quartz with a known elastic modulus. The reduced modulus of each indent was determined by the Hysitron software using the Oliver-Pharr method [68].

3.4. Microstructure characterization

3.3.1. X-ray diffraction

X-ray diffraction (XRD) was used extensively to determine the crystal structure and microstructure of samples. A Rigaku SmartLab diffractometer with a Cu K α source was used in the Bragg-Brentano geometry. Powder samples were placed in a glass slide with a shallow

well that allowed the top surface of the powder to be level with the top of the slide. Bulk samples were placed on a flat glass slide and the diffractometer's automatic alignment features used to adjust the height of the stage and correct for any slight non-levelness of the sample.

Phase analysis was done using the Rigaku PDXL and PANalytical HighScore software with the ICDD PDF-4 database. These software packages use the peak position and intensity to determine the most likely phases from the database given filters such as the known elemental composition of the sample.

For quantitative line profile measurements by XRD, the instrumental broadening contribution to the pattern must be subtracted. A standard material, coarse-grained aluminum oxide (NIST 1976a) was used to determine the instrumental profile as a function of angle. The results were fitted to the Caglioti formulae [69]:

$$FWHM^2 = W + V \tan \theta + U \tan^2 \theta \quad (3.4)$$

$$\eta_{Lorentz} = a + b \theta + c \theta^2 \quad (3.5)$$

where W, V, U, a, b, and c are constants, fit to the diffraction profile of the alumina standard using the whole powder pattern modeling technique described below. 3.4 describes the instrumental broadening, while 3.5 describes the Lorentzian fraction of a pseudo-Voigt curve, used by the pattern modeling software to model the instrumental profile more accurately.

Basic measurements of the microstructure were done using the Scherrer formula [70] to estimate the crystallite size (which was assumed to be equivalent to the grain size)

$$d = \frac{K\lambda}{B \cos \theta} \quad (3.6)$$

where K is a shape factor between 0.9 and 1.0 (with 1.0 used in this work), λ is the x-ray wavelength, θ is the location of the center of the peak, and B is the FWHM of the peak after subtracting the instrumental contribution. To determine the microstrain in the samples, the Williamson-Hall method was employed. The microstrain is given by the slope of the linear fit of $(B \cos \theta)$ vs $(\sin \theta)$ [70,71]. Despite significant scatter in the data leading to an apparently poor linear fit for most samples, this method was found to be the most reliable and repeatable.

For more detailed analysis of the microstructure, a whole powder pattern modeling (WPPM) method was employed, using the PM2K software [72]. In this technique, multiple models describing the instrumental broadening, crystal structure, stacking and twin faults, deformation by dislocations, and crystallite size and shape are convoluted and simultaneously refined using a non-linear least squares fit to the experimental data. This was used for accurate measurements of the lattice parameter and stacking fault probability, used to calculate the stacking fault energy.

The stacking fault energy (SFE) of the alloys was also calculated using XRD data with the equation [73]:

$$\gamma = \frac{K_{111}\omega_0 G_{(111)} a A^{-0.37} \langle \epsilon^2 \rangle}{\pi\sqrt{3} \alpha} \quad (3.7)$$

where $K_{111}\omega_0$ is a proportionality constant equal to 6.6 for fcc metals, $G_{(111)}$ is the shear modulus in the (111) plane, calculated using the single crystal elastic stiffness coefficients as

$(1/3)(c_{44} + c_{11} - c_{12})$, a is the lattice parameter, A is the Zener elastic anisotropy, $2c_{44}/(c_{11} - c_{12})$, α is the stacking fault probability measured using PM2K, and $\langle \epsilon^2 \rangle$ is the mean square microstrain, calculated from the Williamson-Hall microstrain, e , with the relation $e = 1.25 \langle \epsilon^2 \rangle^{1/2}$ [74].

3.3.2. Optical microscopy

Optical microscopy was used for grain size measurements of bulk samples. Samples were polished using conventional metallographic methods (SiC papers and alumina suspensions), then etched for several minutes using “Kalling’s 2” solution, as described in ASTM standard E407-07: 2 g CuCl_2 , 40 mL HCl, and 40 mL ethanol [75].

3.3.3. Electron microscopy

Most scanning electron microscopy (SEM) analysis was done using a Hitachi S3200 SEM with a thermionic source under high vacuum conditions, with accelerating voltages between 10 – 30 kV used. It was equipped with an Everhart-Thornley secondary electron detector, Robinson backscattered electron detector, and Oxford energy dispersive spectrometer (EDS). EDS works by measuring the energy and intensity of x-rays generated by beam electrons ejecting inner shell electrons from the atoms of the sample. These x-rays have consistent energies, characteristic to each element. Using the energies and intensities, the approximate composition of the sample can be calculated [76]. The 4pi Revolution software was used for image acquisition and quantitative EDS analysis.

Electron backscatter diffraction (EBSD) and sample preparation for transmission electron microscopy were done using an FEI Quanta 3D FEG with field emission source, focused ion beam (FIB) column, and Oxford Nordlys EBSD detector. Samples for EBSD analysis were polished using SiC papers, with a final polish using 50 nm alumina suspension in a vibratory polisher. Finally, they were etched using the method described in the optical microscopy section above. In EBSD analysis, a CCD camera is used to image the patterns of Kikuchi lines generated from the diffraction of electrons in a highly tilted sample. If the crystal structure of the material is known, software can index the patterns to determine the orientation of the crystals, generating a map of phases and grain orientation [76]. TEM samples were prepared using the *in situ* lift-out method. First, a small quantity of Pt-containing organometallic gas is injected above the sample and the FIB with 30 kV Ga ions is used to induce deposition of Pt[77] over the region of interest. This protects the sample from damage during the remainder of the process[78]. Next, the FIB is used to sputter away material from around the sample, creating a thin ($<1\ \mu\text{m}$) rectangular ($\sim 15 \times 10\ \mu\text{m}$) section. Pt is used to attach the sample to a small needle, and it is then cut away from the material. While attached to the needle, the sample is moved to a copper TEM grid, attached using Pt, and removed from the needle. Finally, it is thinned using the FIB, with reduced beam current and voltage to prevent damage, until electron-transparent [79].

In addition to the FIB lift-out method, samples of bulk materials were prepared for TEM analysis by twin-jet electropolishing. Small samples were cut and mechanically polished to $< 100\ \mu\text{m}$ thickness. They were then polished using a Tenupol polishing machine

with a solution of methanol and perchloric acid chilled to near the freezing point of methanol with liquid nitrogen. TEM analysis was done using a JEOL 2000FX and FEI Titan 80-300, both operated at an accelerating voltage of 200 kV. The FEI Titan was equipped with a spherical aberration corrector and Bruker EDS system.

3.5. Magnetic testing

Magnetic measurements were made using a Quantum Design MPMS superconducting quantum interference device vibrating sample magnetometer (SQUID-VSM). The MPMS uses a superconducting helium-cooled magnet to apply a magnetic field up to ± 70 kOe at temperatures from 1.8 to 400 K. Typical measurements were magnetic moment versus applied field at constant temperature and magnetic moment versus temperature at constant applied field. Data analysis to convert from moment (emu) to mass magnetization (emu/g) and calculation of coercivity, remanence, saturation magnetization, and energy product were done using Origin 9.5.

4. MECHANICAL PROPERTIES AND STACKING FAULT ENERGIES OF NiFeCrCoMn HIGH ENTROPY ALLOY

This chapter was originally published by A. J. Zaddach, C. Niu, C. C. Koch, and D. L. Irving in *JOM* Volume 65, Pages 1780-1789 (2013). A. Zaddach conducted sample preparation, mechanical tests, and x-ray diffraction measurements and analysis.

4.1. Abstract

Materials with low-stacking fault energies have been long sought for their many desirable mechanical attributes. Although there have been many successful reports of low stacking fault alloys (for example Cu-based and Mg-based), many have lacked sufficient strength to be relevant for structural applications. The recent discovery and development of multi-component equiatomic alloys (or high entropy alloys) that form as simple solid solutions on ideal lattices has opened the door to investigate changes in stacking fault energy in materials that naturally exhibit high mechanical strength. We report in this paper our efforts to determine the stacking fault energies of two to five component alloys. A range of methods that include ball milling, arc melting and casting are used to synthesize the alloys. The resulting structure of the alloys is determined from x-ray diffraction measurements. First principles electronic structure calculations are employed to determine elastic constants, lattice parameters, and Poisson's ratios for the same alloys. These values are then used in conjunction with x-ray diffraction measurements to quantify stacking fault energies as a function of number of components in the equiatomic alloys. We show that the stacking fault

energies decrease with number of components. Non-equiatomic alloys are also explored as a means to further reduce stacking fault energy. We show that this strategy leads to a means to further reduce the stacking fault energy in this class of alloys.

4.2. Introduction

In many conventional structural materials, strength and ductility are mutually exclusive. When the strength is increased, such as by refining the grain size, there often is a corresponding decrease in ductility, which limits the use of the strengthened material for structural applications [61]. In ultrafine grain (UFG) and nanocrystalline (NC) materials, this is attributed to their poor capacity for accumulating dislocations in the small grains, resulting in a lack of work hardening [57,61]. Recently, significant advances have been made in developing UFG/NC materials with improved ductility by selecting alloys with low stacking fault energy (SFE) [57,58,61,80–83]. High SFE materials deform by dislocation glide and dissociation into partial dislocations is difficult. In low SFE materials, dissociation into partial dislocations is more energetically favorable and the spacing between the partial dislocations (the width of the stacking fault) is larger. As the spacing increases, cross-slip and climb becomes more difficult, increasing strength. Low SFE materials are also more likely to deform by twinning, increasing dislocation storage capacity, strain hardening rate, and ductility [54,57,58,80,81]. High-density “bundles” of nanoscale twins have been observed after deformation in low SFE copper alloys [84]. Regions containing high densities of

nanoscale spaced stacking faults that provide a similar strengthening effect have been observed in low SFE magnesium alloys [85].

To date, much of the research on improving strength and ductility by reducing SFE has focused on binary and ternary Cu-based alloys and multi-component Mg-based alloys. The main reason for this attention is the well-established ability of some alloying elements to form solid solutions in Cu and Mg and significantly lower the stacking fault energy. While some impressive results have been obtained, the strength of most of the alloys is still relatively low. Cu–10wt%Zn with a grain size of 110 nm retains elongation to failure of greater than 6%, but the yield strength is improved to only ~600 MPa [61]. An alternative, and possibly more desirable system, would be one that, like the Cu-based alloys, can form an fcc solid solution over a wide range of compositions and has low SFE but also retains high intrinsic strength.

Recently, a new class of multi-component alloy systems has been developed in which the design is based not on adding solutes to a single “base” element, but rather on choosing elements that will form solid solutions when mixed at near-equiatomic concentrations. These “high-entropy alloys” (HEAs) meet these criteria and are found to form solid solutions. This behavior has been attributed to the large configurational entropy when five or more elements at near-equiatomic ratios are mixed together [2]. Elements likely to form as an HEA solid solution and which lattice is likely to form will now be briefly reviewed.

A fundamental understanding of the mechanisms of phase stability of HEAs is still a topic of active research. Guo *et al.* demonstrated that elements likely to form HEAs have

near-zero enthalpies of mixing and have very small differences in atomic radius [86]. The small enthalpy of mixing allows the configurational entropy to dominate the free energy and it has been proposed that the system behaves, in this case, more like an ideal solution. Otto *et al.* recently published a systematic investigation on the effect of entropy on phase stability of HEAs [27]. The authors demonstrated that high configurational entropy is not the only sufficient criterion to predict whether an equiatomic multicomponent alloy will form as a single-phase solid solution. In their study, they found only NiFeCrCoMn alloys to be a single-phase fcc solid solution and a HEA. These findings are consistent with the work of Guo *et al.* as all the enthalpies of mixing in the respective binary alloys are relatively small and the atoms are similar in size. The authors then replaced individual elements in an equiatomic NiFeCrCoMn alloy one at a time with elements that have the same room temperature crystal structure, similar atomic size, and similar electronegativity as compared to the elements being replaced. All other substitutions to the NiFeCrCoMn alloy led to a multi-phase alloy. Although the replacement elements were “similar” according to Hume-Rothery rules, the authors found that the substituted elements had a stronger propensity to form secondary phases or intermetallics in their respective binary alloys. This led the system to act less as an ideal solution and resulted in the formation of multi-phase alloy with a reduced overall entropy [27].

There has also been interest in finding descriptors to predict the likely lattice that the solid solution will form upon. One descriptor that has been reasonably successful in predicting the lattice structure is the average valence electron concentration (VEC) [42]. fcc

phases were determined to be more stable at higher VEC (≥ 8) while bcc phases at lower VEC (< 6.87). On the boundary between fcc and bcc (VEC=8) the systems were found to be predominantly fcc but in some situations bcc has been seen in minute amounts.

To explore the physical properties of an HEA we have implemented an integrated approach that combines results from experiment and first principles electronic structure methods. Ni, Fe, Cr, Co and Mn were chosen as the components of the HEA studied herein. The small size difference, small enthalpies of mixing, VEC and previous findings suggest that this forms as a solid solution on the fcc lattice. Additionally, binary (NiFe), ternary (NiFeCr), and quaternary (NiFeCrCo) alloys form fcc solid solution phases. This allows us to explore the evolution of a variety of properties, such as elastic constants, lattice parameters, and stacking fault energies, as a function of the number of components. We show the atomic radii of these elements from the literature in Table 4.1. The VEC of NiFeCrCoMn is 8, and is found to be solely fcc in both previous studies and our current work [1,27].

Table 4.1. Atomic radii and valence electron concentration of pure metals [87].

Element	Ni	Fe	Cr	Co	Mn	Average
Atomic Radius (pm)	124.6	127.4	128.2	125.2	126.4	126.4
VEC	10	8	6	9	7	8

In addition to the equiatomic alloys, we also produced some off stoichiometry 5-component alloys to determine how the SFE and other properties change with composition. The alloys produced for this study are listed in Table 4.2 along with their average valence

electron concentration and the entropy of mixing for the ideal solid solution, given by

$$\Delta S = -R \sum x_i \ln x_i, \text{ where } R \text{ is the ideal gas constant and } x_i \text{ is the concentration of component}$$

i. In this paper, we have adopted the following naming convention: Alloy names without subscripts are equiatomic; in alloy names with subscripts, the subscript value is the concentration in atomic percent.

Table 4.2. Composition, average VEC, and ideal entropy of mixing of alloys produced.

Alloy	VEC	ΔS_{mix} (J K ⁻¹ mol ⁻¹)
NiFe	9	5.76
NiFeCr	8	9.13
NiFeCrCo	8.25	11.53
NiFeCrCoMn	8	13.38
Ni ₂₆ Fe ₂₀ Cr ₁₄ Co ₂₀ Mn ₂₀	8.24	13.23
Ni ₂₃ Fe ₂₀ Cr ₁₇ Co ₂₀ Mn ₂₀	8.12	13.34
Ni ₁₄ Fe ₂₀ Cr ₂₆ Co ₂₀ Mn ₂₀	7.76	13.23
Ni ₁₄ Fe _{21.5} Cr _{21.5} Co _{21.5} Mn _{21.5}	7.85	13.28

4.3. Methods

4.3.1. Experimental

Alloy powders were prepared by mechanical alloying of elemental powders in a high-energy ball mill. Powders of better than 99% purity were loaded into a stainless steel vial with stainless steel balls in a high-purity argon atmosphere. A 10:1 ball-powder weight ratio was used. Approximately 0.7 wt% dodecane (2 drops) was added to four- and five-component alloys as a process control agent to minimize cold welding. Binary (NiFe) alloys

were milled in a modified SPEX 8000 mixer mill cooled by liquid nitrogen for 4 hours. Ternary (NiFeCr) alloys were milled at liquid nitrogen temperatures for 8 hours, followed by 17 hours of milling at room temperature with forced-air cooling. Quaternary (NiFeCrCo) and quinary (NiFeCrCoMn) samples were milled with forced-air cooling for 24-29 hours. Before any analysis, the dodecane was removed by evaporation in a vacuum chamber for at least 18 hours.

Bulk samples were prepared by arc melting. Pure (better than 99%), bulk elements were melted on a water-cooled copper hearth in a Ti-gettered argon atmosphere. Ingots were flipped and remelted at least three times to ensure the elements were well mixed. Samples were drop cast into a water-cooled 7 mm diameter cylindrical copper mold.

X-ray diffraction (XRD) analysis was conducted using a Rigaku Smartlab diffractometer with Cu $K\alpha$ radiation. The PM2K software was used to analyze the diffraction patterns using the Whole Powder Pattern Modeling algorithm [72]. With this method, multiple models relating the microstructure and crystallography of the sample are convoluted and simultaneously refined to fit the measured pattern using a non-linear least squares algorithm. The software accounts for instrumental broadening and can correct for sample position errors. PM2K was used to measure the lattice parameter, dislocation density, grain size, twin fault probability, and stacking fault probability [72]. A Lorentzian peak function was fit to each peak in the diffraction profile and the widths used to determine the microstrain using the Williamson-Hall method [71]. The microstrain was converted to mean-square strain as described by Klug and Alexander [74]. The elastic constants were calculated

using density functional theory as described in the next section. The stacking fault energy is then calculated as:

$$\gamma = \frac{K_{111}\omega_0 G_{(111)} a_0 A^{-0.37}}{\pi\sqrt{3}} \cdot \frac{\epsilon^2}{\alpha} \quad (4.1)$$

where $K_{111}\omega_0$ is assumed to be a constant 6.6 for all fcc materials, $G_{(111)}$ is the shear modulus in the (111) plane, a_0 is the lattice parameter, A is the Zener elastic anisotropy:

$2C_{44}/(C-C_{12})$, ϵ^2 is the mean square microstrain, and α is the stacking fault probability [73]. XRD measurements for lattice parameters of the cast alloys were performed after cold rolling to increase the surface area of the sample.

Microhardness tests were conducted on powder samples that were fixed to a glass slide using epoxy then polished. Cast samples were annealed at 1000 °C for 24 hours, cut using a low-speed diamond saw, mounted in epoxy, and polished. Testing was done with a 50 g load. At least 10 measurements were taken on each sample.

Young's modulus of the as-milled powders was estimated from the reduced Young's modulus determined by nanoindentation using a Hysitron Triboindenter and a load of 5 mN. Samples were prepared as described for microhardness tests. Young's modulus of the sample is calculated from the reduced modulus using:

$$\frac{1}{E_r} = \left(\frac{1-\nu^2}{E} \right)_{sample} + \left(\frac{1-\nu^2}{E} \right)_{indenter} \quad (4.2)$$

The modulus and Poisson's ratio of the indenter were 1140 GPa and 0.07, respectively. A range of values of the Poisson's ratio for the alloys was obtained computationally.

The grain size of the cast alloys was determined by optical microscopy and the line-intercept method after polishing and etching by immersion in solutions of CuCl_2 , HCl, and methanol and FeCl_3 , CuCl_2 , HCl, HNO_3 , and ethanol for the NiFeCrCo and NiFeCrCoMn alloys, respectively.

4.3.2. Computational

Two methods were used to investigate the physical properties of these solid solution alloys. Both are based on density functional theory (DFT). The first method was the exact muffin-tin orbital (EMTO) [88,89] method combined with coherent potential approximation (CPA) [90,91]. The second method was a plane wave-pseudopotential approach as implemented in the Vienna *ab initio* simulation packages (VASP) version 5.2.12 [92–95]. VASP uses periodic boundary conditions. To best approximate the random solid solution, special quasi-random structures (SQSs) [96] were generated using the tool in the Alloy Theoretic Automated Toolkit (ATAT) [97].

The EMTO method is an improved screened Korringa-Kohn-Rostoker (KKR) method that uses optimized overlapping muffin-tin potentials to describe the actual crystal potential and calculates system energies with higher accuracy than the conventional muffin-tin orbital (MTO) method [98]. This method is combined with the CPA technique to treat systems with

substitutional disorder. The EMTO-CPA method proved a powerful tool in the *ab initio* study of solid solutions, e.g., mechanical properties [99] and stacking fault energies[100] of stainless steels. In the present EMTO-CPA calculation of HEAs, the one-electron equations were solved using the frozen-core approximation. The Green's function was calculated for 16 complex energy points. The basis set included *s*, *p*, *d* and *f* orbitals. The PBE version of GGA exchange-correlation functional was applied [101,102]. The magnetic disorder in HEAs was treated by the disordered local moments (DLM) method [103].

To consider the influence of the lattice displacement on DFT calculations, we also performed similar calculations using VASP+SQS. Projector augmented-wave (PAW) pseudopotentials [104,105] and the PBE version of generalized gradient approximation (GGA-PBE) were used in VASP calculations. There are 10, 8, 6, 9, and 7 valence electrons for elements Ni, Fe, Cr, Co, and Mn, respectively. In addition to these valence electrons the 3p electrons of Fe, Cr, and Mn are also treated explicitly in the PAW pseudopotentials used in this work. Non-collinear spin and spin-orbit coupling was included in the VASP calculations. Both spin aligned and random moments are assigned to atoms within the SQS. The lowest energy is found to be ferromagnetic at 0 K, which differs from the experimentally measured paramagnetic state. The impact of the ferromagnetism in the predicted properties of VASP will be discussed. The cut-off energy for plane waves was set to 350 eV for all calculations. The k-point mesh was selected based on what converged the total energy to ~ 1 meV/atom. This resulted in a 7x4x4 and 4x7x7 Γ -centered mesh for the 24 and 20 atom SQSs, respectively. The SQSs were generated by *mcsqs* algorithm included in the ATAT

package. The generation of a SQS was based on lattice geometry, specifically the pair correlation function between lattice sites. Different atomic configurations were created and the sum of pair correlation functions on each site was calculated. A structure in which the sum of pair correlation functions on each site is closer to zero was considered a better SQS. The SQSs of the quaternary and quinary alloys contained 24 atoms and 20 atoms, respectively. Table 4.3 contains the atomic positions and site populations for the four and five component fcc SQSs used in this work. There are 46 and 90 pair (out to third nearest neighbor) and triplet (out to second nearest neighbor) correlation functions to report for the four and five component systems presented in Table 4.3. We note that none of the absolute magnitudes of the pair correlation function exceed 0.05 and 0.03 for the four and five component SQSs, respectively, and none of the triplet correlation functions exceed an absolute magnitude of 0.04 and 0.06 for the four and five component SQSs, respectively. The weighted average of the pair and triplet correlation functions were at least one order of magnitude less than these reported maximum values. Although the SQSs contain a small number of atoms, these structures have proven to provide a means to accurately predict physical and elastic properties of alloys [106,107].

Table 4.3. SQS for NiFeCrCo and NiFeCrCoMn alloys containing 24 and 20 atoms, respectively.

Initial atomic positions are in Cartesian coordinates scaled by the lattice parameter.

	NiFeCrCo ($N=24$)	NiFeCrCoMn ($N=20$)
Lattice vectors	(0.5, -0.5, -1.0) (-1.5, -1.5, 0.0) (-1.5, 1.5, -1.0)	(0.5, 2.0, -0.5) (0.5, -0.5, 2.0) (1.0, -0.5, -0.5)
Atomic positions	Ni (3.0, 0.0, 3.0) Ni (0.5, -2.0, 3.5) Ni (1.5, -3.0, 3.5) Ni (0.0, -1.5, 2.5) Ni (2.0, -0.5, 1.5) Ni (0.5, -0.5, 1.0) Fe (1.0, -1.0, 4.0) Fe (2.5, 0.5, 2.0) Fe (1.0, -1.0, 2.0) Fe (0.0, -3.0, 3.0) Fe (2.5, -1.0, 4.5) Fe (1.0, -2.5, 2.5) Cr (2.0, -2.0, 4.0) Cr (0.5, -0.5, 3.0) Cr (1.5, 0.0, 2.5) Cr (2.5, -1.0, 2.5) Cr (1.0, 0.5, 1.5) Cr (1.0, 0.5, 3.5) Co (1.5, 1.5, 2.0) Co (2.0, -0.5, 3.5) Co (1.5, -1.5, 3.0) Co (2.0, -2.0, 2.0) Co (2.0, 1.0, 3.0) Co (3.0, 1.5, 2.5)	Ni(0.75, 0.75, -0.50) Ni(1.25, 2.75, -1.00) Ni(2.25, 1.00, -0.25) Ni(0.25, 2.00, 0.75) Fe(1.50, 2.75, -2.25) Fe(0.75, 2.00, -1.75) Fe(1.00, 2.75, 0.25) Fe(1.75, 1.00, 2.25) Cr(2.00, 2.25, -0.25) Cr(0.75, 2.75, 1.50) Cr(1.75, 2.25, 1.00) Cr(0.75, 1.50, 2.75) Co(0.50, 0.75, 0.75) Co(1.25, 1.50, 0.25) Co(2.00, 1.00, 1.00) Co(1.00, 1.50, 1.50) Mn(1.75, 1.50, -2.25) Mn(2.50, 3.00, 0.50) Mn(1.50, 1.50, -1.00) Mn(0.50, 2.00, -0.50)

Both methods were used to determine the lattice constant, elastic constants, and Poisson's ratio for the alloys studied herein. The lattice constants for each alloy from DFT

calculations are compared to experimental results from our research and the literature. The elastic constants were used to determine the first-principles polycrystalline elastic properties, e.g., Young's modulus and Poisson's ratio. Together with the experimental results, the Poisson's ratio was applied for the measurement of the Young's modulus with Eq (4.2). As many of the SFEs are small, the relative energies between important phases used in the axial interaction method to predict SFEs [108,109] (fcc, hcp, and dhcp) are also expected to lead to small differences in energy. When this is the case, factors, such as zero point energy differences, may play a more significant role in the prediction of the SFE. To avoid the added computational expense of these vibrational calculations, we calculate the SFEs by combining experimental measurements from XRD with the predicted elastic properties through equation 4.1. Explicit calculation of the SFEs will be fully explored in a separate publication.

4.4. Results and discussion

4.4.1 X-ray diffraction

Figure 4.1 shows the XRD patterns of the as-milled equiatomic alloys and the $\text{Ni}_{14}\text{Fe}_{20}\text{Cr}_{26}\text{Co}_{20}\text{Mn}_{20}$ alloy. All of the alloys are single-phase and fcc. Despite the average VEC of the $\text{Ni}_{14}\text{Fe}_{20}\text{Cr}_{26}\text{Co}_{20}\text{Mn}_{20}$ alloy being less than 8, it still forms a single-phase fcc solid solution by mechanical alloying.

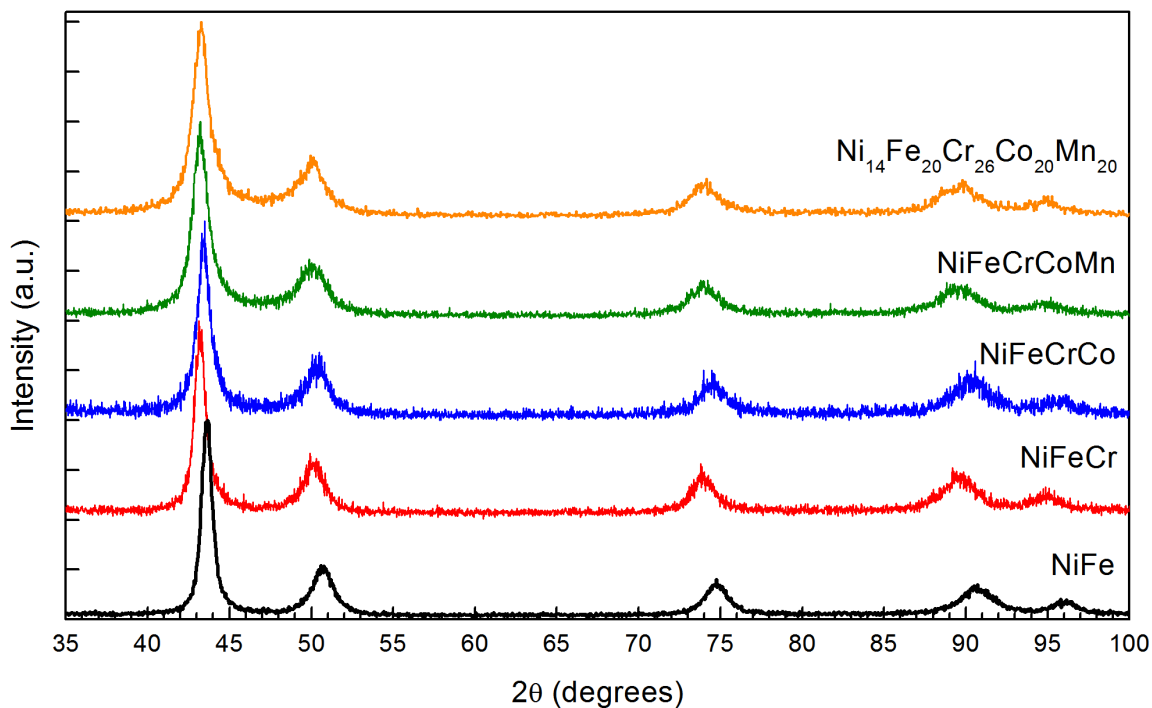


Figure 4.1. XRD patterns of as-milled equiatomic NiFe, NiFeCr, NiFeCrCo, and NiFeCrCoMn.

The lattice parameters of the four and five components were determined directly from the XRD measurements and first principles calculations. For NiFeCrCo the lattice parameters measured by XRD were 3.613 and 3.575 Å for the as-milled and cast samples, respectively. First principles calculations predict lattice parameters of 3.58 and 3.54 Å from EMTO-CPA and VASP+SQS methods, respectively. Both results are within 1% of the cast results and are consistent with the measured lattice parameters presented in reference [110]. For the NiFeCrCoMn alloy the lattice parameters from XRD were measured to be 3.624 and 3.597 Å for the as-milled and cast samples, respectively. The trends in both first principles

agree with the experimental trend of increasing lattice parameter with increasing number of components. The lattice parameter predictions for NiFeCrCoMn from first principles calculations were 3.60 and 3.54 Å for EMTO-CPA and VASP+SQS methods, respectively, with the error on the order of 1.6% relative to the cast lattice parameter. The lattice parameter for the off stoichiometry $\text{Ni}_{14}\text{Fe}_{20}\text{Cr}_{26}\text{Co}_{20}\text{Mn}_{20}$ alloy is found to be 3.627 and 3.60 Å from XRD of the as-milled alloy and EMTO-CPA, respectively, which is an error of 0.7%. The lattice parameters of the as-milled alloys are expected to be higher as a result of the non-equilibrium processing conditions and high defect density [111].

4.4.2 Single crystal elastic constants

Elastic properties of a crystal can be expressed by the elasticity tensor. For cubic structures, there are three independent elastic constants: C_{11} , C_{12} and C_{44} . C_{11} and C_{12} can be derived from the bulk modulus, B , and the tetragonal shear modulus, C' , given that $B = (C_{11} + 2C_{12})/3$ and $C' = (C_{11} - C_{12})/2$. The bulk modulus was obtained by fitting the energy-volume data to the Birch-Murnaghan equation of state. For the tetragonal shear modulus C' and C_{44} we applied a volume-conserving orthorhombic deformation ε_0 and a volume-conserving monoclinic deformation ε_m on the fcc lattice [105], respectively. These relationships are:

$$\varepsilon_0 = \begin{pmatrix} 1+\delta & 0 & 0 \\ 0 & 1-\delta & 0 \\ 0 & 0 & (1-\delta^2)^{-1} \end{pmatrix}; \varepsilon_m = \begin{pmatrix} 1 & \delta & 0 \\ \delta & 1 & 0 \\ 0 & 0 & (1-\delta^2)^{-1} \end{pmatrix} \quad (4.3)$$

where δ was between 0.00 and 0.05 in increments of 0.01. The values of C' and C_{44} were determined by fitting the calculated energies to $E = E_0 + 2VC'\delta^2$ and $E = E_0 + 2VC_{44}\delta^2$ [112]. In these expressions, E is the total energy of the strained system from first principles, E_0 is the energy at the equilibrium volume, and V is the volume of the cell. The elastic constants were determined using EMTO-CPA and VASP for NiFeCrCo and NiFeCrCoMn while the elastic constants for off stoichiometry alloys were determined from EMTO-CPA alone. A strain range no greater than 5% was used in the EMTO-CPA and the VASP calculations to determine the bulk modulus through fitting of results to the Birch-Murnaghan equations of state. As shown in Figure 4.2, the calculated elastic constants and bulk moduli depend on the first principles method implemented. The deviation between results of the two methods increases for NiFeCrCoMn. We also compare our results of the four-component systems to Tian *et al.* who calculated the elastic constants of NiFeCrCo using the EMTO-CPA code [113]. Differences between our results and those published are small and attributed to the setup of the calculations. Tian *et al.* used soft core, 240 k-points, and a screening parameter of 0.6. In our calculations we implemented frozen core, 419 k-points, and a screening parameter of 0.9.

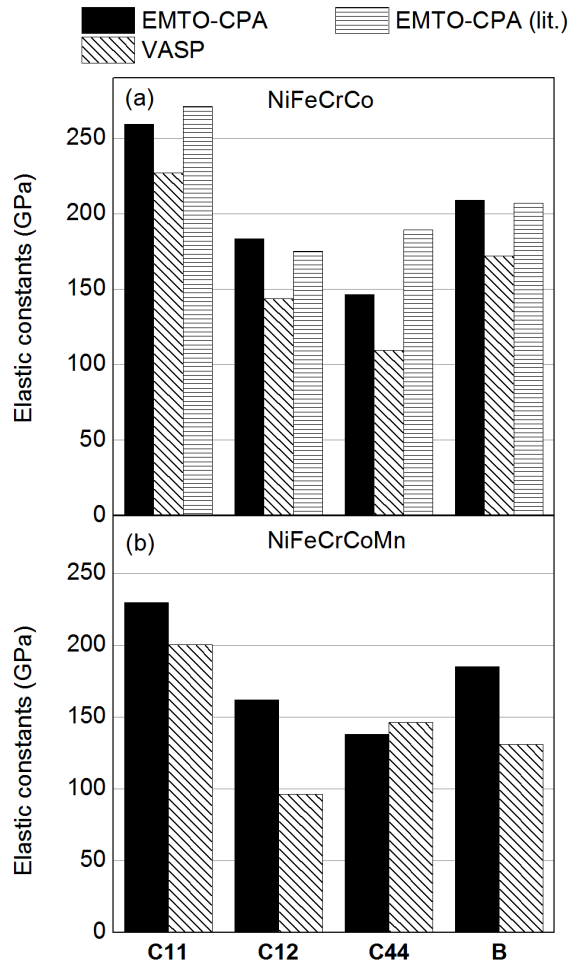


Figure 4.2. Elastic constants of equiatomic NiFeCrCo (a) and NiFeCrCoMn (b) [46].

Deviations in the elastic constants between VASP and EMTO-CPA for the four and five component alloys were explored and are believed to be partially due to the magnetic configuration in the calculation. VASP predicts ferromagnetic, while EMTO-CPA is run with DLM approximating the experimental paramagnetic state. To the validity of this assertion,

EMTO-CPA was run with a ferromagnetic configuration. This ferromagnetic EMTO-CPA calculation predicts a lower total energy at 0 K and elastic coefficients in closer agreement to the VASP calculations. The elastic constants from our EMTO-CPA and VASP calculations will be used to determine polycrystalline constants, which will then be used with Eq (4.1) to determine the SFEs of the alloys. Although there are differences in the predicted elastic constants, it will be shown that these have smaller impact on the SFEs determined by this process.

4.4.3 Polycrystalline elastic constants

We derived the polycrystalline elastic properties using the elastic constants and the Voigt-Reuss (V-R) averaging method [114]. According to the V-R method, the polycrystalline bulk modulus is the same as the single crystalline bulk modulus from DFT calculation, while the shear modulus G can be given by the upper (G_V) and lower (G_R) bounds:

$$G_V = \frac{(C_{11} - C_{12} + 3C_{44})}{5}; G_R = \frac{5(C_{11} - C_{12})C_{44}}{4C_{44} + 3(C_{11} - C_{12})} \quad (4.4)$$

The shear modulus G can be estimated as $(G_V + G_R)/2$, according to the Hill averaging method [110]. Poisson's ratio and Young's modulus E for an isotropic material can be derived from the bulk modulus B and shear modulus G :

$$\nu = \frac{3B - 2G}{2(3B + G)}; E = \frac{9BG}{3B + G} \quad (4.5)$$

Table 4.4 shows the calculated values of Poisson's ratio assuming a Hill average. The values of Poisson's ratio of NiFeCrCo from the two first principles methods are very close. As noted previously, the elastic constants of NiFeCrCo from the two methods differ, which is not surprising as there are differences in the bulk modulus (208 vs. 171 GPa from EMTO and VASP, respectively). This implies that the deviations of the elastic constants are cancelled during the calculation of Poisson's ratio in Eq (4.4) and (4.5). The Hill average of Poisson's ratio of NiFeCrCoMn differ as much as ~42% between the two methods, which arises from the deviation of elastic constants. As noted previously, this may be partially related to the differences in the magnetic state.

Table 4.4. Poisson's ratio of NiFeCrCo and NiFeCrCoMn from DFT calculations.

	Hill average
NiFeCrCo (EMTO-CPA)	0.319
NiFeCrCo (VASP)	0.311
NiFeCrCoMn (EMTO-CPA)	0.313
NiFeCrCoMn (VASP)	0.204

Table 4.5 shows the values of Young's modulus from our calculations and experiments. The range of values from the nanoindentation experiments was determined by converting the reduced modulus using the Hill average of Poisson's ratio from the DFT calculations. VASP and EMTO results are presented for the four-component alloy but only EMTO-CPA results are included for the five-component alloy. While there is closer agreement between theory and experiment for the NiFeCrCo alloy, the measured Young's

modulus of the NiFeCrCoMn alloy is substantially lower than the predicted result. It should be noted that the bulk moduli calculated using VASP for the four- and five-component alloys presented previously in Figure 4.2 show a decrease in the bulk modulus from 172 to 131 GPa. With a more physical Poisson's ratio for the five component alloy (i.e. closer to the 0.311 predicated for the four-component alloy) and the following relationship between Bulk modulus and Young's modulus for an isotropic solid: $E = 3B(1 - 2\nu)$, we would find these results closer to experiment with Young's moduli of 195 and 149 GPa for the four- and five-component alloys, respectively. Due to the scatter in the measurement of the reduced modulus, we consider these in good agreement with experimental measurements from nanoindentation.

Table 4.5. Young's modulus of NiFeCrCo and NiFeCrCoMn from DFT calculations and experiment.

	E_{Hill} (GPa)
NiFeCrCo (EMTO-CPA)	225
NiFeCrCo (VASP)	195
NiFeCrCo (nanoindentation + EMTO)	171
NiFeCrCo (nanoindentation + VASP)	172
NiFeCrCoMn (EMTO-CPA)	207
NiFeCrCoMn (nanoindentation + EMTO)	137

4.4.4. Stacking fault energy

Figure 4.3 shows the ratio of the mean square microstrain to the stacking fault probability in the as-milled alloys as measured using XRD. From Eq (4.1), this value is related to the stacking fault energy by the elastic constants and the lattice parameter. From

these results, we can predict that the SFE of the four- and five-component alloys will be nearly an order of magnitude lower than that of NiFe.

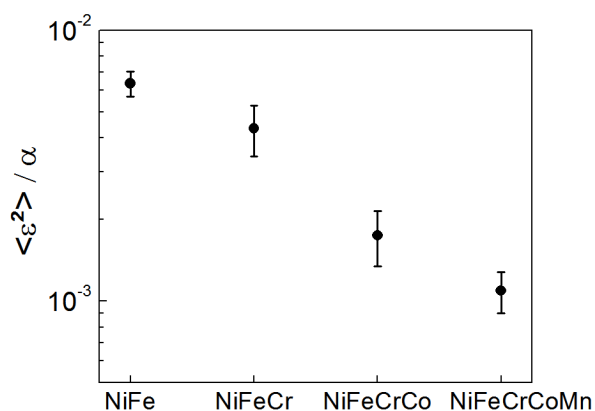


Figure 4.3. Ratio of mean-square microstrain to stacking fault probability for NiFe, NiFeCr, NiFeCrCo, and NiFeCrCoMn. Error bars represent error from the stacking fault probability measurement.

Table 4.6 shows the stacking fault energy of the four- and five- component alloys measured using the x-ray stacking fault probability and elastic constants determined by VASP and EMTO-CPA. No reliable error values can be determined for the measurements. The PM2K software calculates an estimated standard deviation for the stacking fault probability and lattice parameter. Nevertheless, there is likely significant error associated with the microstrain calculation, but the Williamson-Hall method does not provide a way to quantify it. Despite significant differences in the elastic constants of the four-component alloy as determined by VASP and EMTO-CPA, the stacking fault energy measurements

agree to within 0.005 mJ/m^2 , which is well within the measurement limits. As with the Poisson's ratio calculation, there is cancelation of error in these measurements.

Table 4.6. SFEs of NiFeCrCo and NiFeCrCoMn calculated from experimental data of stacking fault probability and DFT calculations of elastic constants.

Alloy	SFE (mJ/m^2) (VASP)	SFE (mJ/m^2) (EMTO-CPA)
NiFeCrCo-1	17.4	17.4
NiFeCrCo-2	34.3	34.3
NiFeCrCo-3	31.7	31.7
NiFeCrCoMn-1	27.3	19.6
NiFeCrCoMn-2	25.5	18.3

Figure 4.4 compares the averages of the measured SFE of the NiFe, NiFeCr, NiFeCrCo, and NiFeCrCoMn alloys produced in this study to literature values of pure Ni and NiFe. Elastic constants used for the XRD measurements of NiFe are from [115]. From these measurements, we can conclude that the multi-component alloys have relatively low stacking fault energies, less than a quarter of the SFE of pure nickel. Nevertheless, these values are still on the same order as or slightly higher than some conventional austenitic stainless steel alloys such as AISI 304L ($\gamma=18 \text{ mJ/m}^2$) and AISI 305 ($\gamma=34 \text{ mJ/m}^2$) [116]. Additionally, the decrease in SFE is smaller with each additional alloying element, suggesting that simply adding more elements may not lead to a substantial reduction of the SFE. These results show that while equiatomic NiFeCrCoMn alloys do have reduced SFE, obtaining SFEs on the order of those seen in common copper alloys ($<15 \text{ mJ/m}^2$) will require finding an optimum

composition or compositions. This is a difficult problem considering the number of elements and the wide range of compositions that are still considered “high-entropy alloys”.

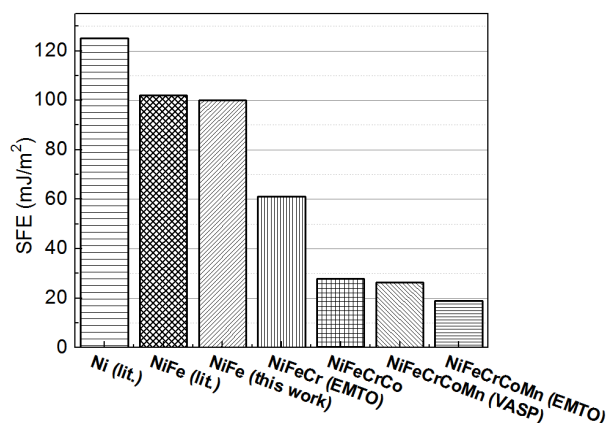


Figure 4.4. SFEs of equiatomic fcc metals from pure Ni to NiFeCrCoMn [73,117].

As Ni is known to have a high SFE, we explored varying its composition while increasing composition of other components in the HEA. We mainly increase the composition of Cr as Ni content is reduced but we also explored raising the composition of all components for a reduced Ni concentration. Figure 4.5 shows the ratio of the mean square microstrain to the stacking fault probability in the as-milled five-component alloys as a function of Ni concentration. From this data, it is expected that the low-Ni alloys will have a much lower SFE than the equiatomic alloy. The SFEs of the non-equiatomic alloys, using elastic constants calculated by EMTO-CPA, are listed in Table 4.7. From these results, we can see that there is a dependence on both the Ni and Cr concentrations. While lowering the Ni concentration independently of the Cr does significantly reduce the SFE, it does not do so

to the same extent as reducing Ni and increasing Cr. The $\text{Ni}_{14}\text{Fe}_{20}\text{Cr}_{26}\text{Co}_{20}\text{Mn}_{20}$ alloy has an extremely low SFE, apparently even lower than Cu-Al-Zn [118] and Cu-Ge [57] alloys. The SFE of various conventional alloys known to have a low SFE are compared to the high-entropy alloys from this study in Figure 4.6.

Table 4.7. SFE of non-equiatomic HEAs.

Alloy	SFE (mJ/m^2)
$\text{Ni}_{26}\text{Fe}_{20}\text{Cr}_{14}\text{Co}_{20}\text{Mn}_{20}$	57.7
$\text{Ni}_{23}\text{Fe}_{20}\text{Cr}_{17}\text{Co}_{20}\text{Mn}_{20}$	19.7
$\text{Ni}_{14}\text{Fe}_{20}\text{Cr}_{26}\text{Co}_{20}\text{Mn}_{20}$	3.5
$\text{Ni}_{14}\text{Fe}_{21.5}\text{Cr}_{21.5}\text{Co}_{21.5}\text{Mn}_{21.5}$	7.7

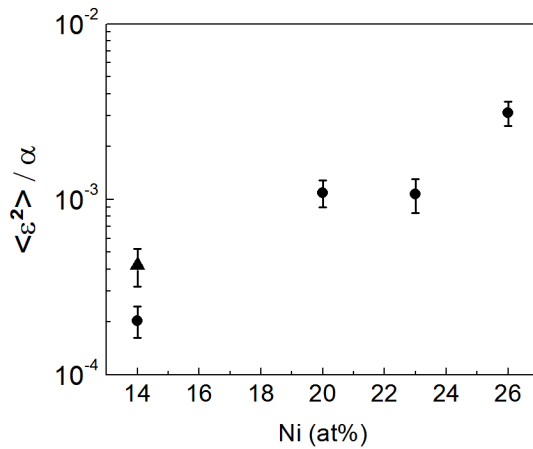


Figure 4.5. Ratio of mean-square microstrain to stacking fault probability for 5-component alloys.

Error bars represent error from the stacking fault probability measurement. Circles represent alloys in which Cr balances the difference in Ni content. The triangle is the alloy in which the concentrations of all other elements are increased equally to balance the Ni.

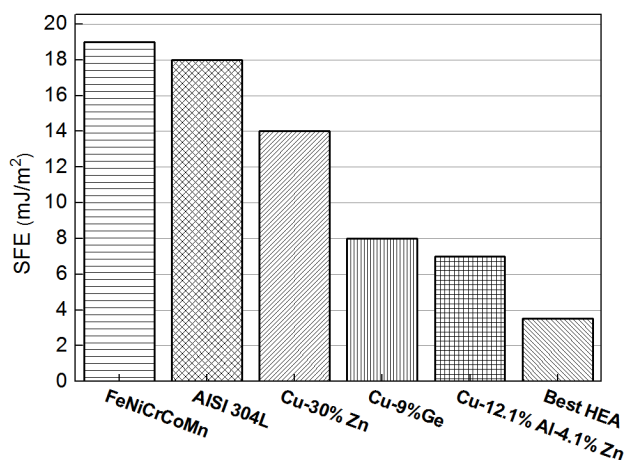


Figure 4.6. SFEs of equiatomic NiFeCrCoMn and Ni₁₄Fe₂₀Cr₂₆Co₂₀Mn₂₀ (“Best HEA”) compared to other low SFE alloys [57,116,118].

4.4.5. Mechanical properties

Gali and George conducted a detailed study of the tensile properties of hot rolled and annealed NiFeCrCo and NiFeCrCoMn [24]. They measured room temperature yield strengths of ~200 MPa in the 4-component alloy and ~300 MPa in the 5-component alloy with grain sizes of 14 and 35 μm , respectively. They also measured uniform elongation of ~40% at room temperature and found that as the test temperature decreased to -196 °C, both the strength and ductility increased. Annealing twins were observed and a high work hardening rate was attributed to the formation of nanoscale deformation twins [24].

Hardness and grain size measurements from the as-milled powders and cast alloys of this study are shown in Table 4.8. Measurement of the grain size of the five-component alloy was difficult due to the large numbers of annealing twins. Additionally, the twin fault probability as measured by XRD in the as-milled four- and five- component samples was

found to be very high, on the order of 0.1. The hardness results show that the nanocrystalline alloys have extremely high strength. Using the common empirical $HV = 3\sigma_y$ relation, the yield strength is likely in the range of 2-2.5 GPa. These results, and those from earlier studies, are consistent with our measurements of low stacking fault energy.

Table 4.8. Hardness and grain size measurements from the as-milled powders and cast alloys.

Material	Hardness (GPa)	Grain size	Std. Dev. of grain size
As-milled NiFeCrCo	6.3 ± 0.1	22 nm	9 nm
As-milled NiFeCrCoMn	7.8 ± 0.2	9.4 nm	5 nm
Cast NiFeCrCo	1.66 ± 0.07	20 μm	--
Cast NiFeCrCoMn	1.42 ± 0.03	49 μm	--

4.5. Summary

The elastic properties and stacking fault energies of multi-component alloys containing Ni, Fe, Cr, Co, and Mn were determined using a combination of density functional theory calculations and experiments. Reasonable agreement between experiments and calculation were found for the lattice parameter and elastic properties, though further experimental work is required to measure values that are completely independent of the calculations. The stacking fault energy of the equiatomic NiFeCrCo and NiFeCrCoMn alloys measured by XRD is approximately 20-25 mJ/m^2 , substantially lower than that of pure Ni and NiFe. These measurements are in agreement with the results of mechanical testing and microstructure characterization by XRD. By altering the composition, the SFE can be tailored to a wide range of values, including low values comparable to or better than

conventional low SFE alloys. The results indicate that fcc high entropy alloys such as NiFeCrCoMn can be engineered to have both high strength and ductility, making them promising candidates for future use as structural materials.

5. TENSILE PROPERTIES OF LOW STACKING FAULT ENERGY HIGH ENTROPY ALLOYS

This chapter was originally published by A. J. Zaddach, R. O. Scattergood and, C. C. Koch in *Materials Science and Engineering: A Volume 636, Pages 373-378 (2015)*. A. Zaddach conducted sample preparation, mechanical tests, and all measurements and analysis.

5.1. Abstract

An equiatomic NiFeCrCoMn alloy, two non-equiatomic NiFeCrCoMn alloys optimized for low stacking fault energy, and an equiatomic NiFeCrCo alloy were produced by arc melting. Samples were homogenized, cold rolled, and annealed at temperatures between 575 and 1100 °C. Samples annealed at a moderate temperature near their recrystallization temperature (625-675 °C) and 1100 °C were cut into flat tensile samples and tested at a strain rate of $7.3 \times 10^{-4} \text{ s}^{-1}$. Equiatomic NiFeCrCo had the highest ductility and toughness after annealing at both temperatures, followed by $\text{Ni}_{18.5}\text{Fe}_{18.5}\text{Cr}_{18.5}\text{Co}_{26}\text{Mn}_{18.5}$. $\text{Ni}_{14}\text{Fe}_{20}\text{Cr}_{26}\text{Co}_{20}\text{Mn}_{20}$ exhibited poor thermal stability, forming σ -phase intermetallics at temperatures below 1100 °C. Observation of the fracture surfaces suggested that the high performance of NiFeCrCo might be due to the absence of oxide particles that form in the Mn-containing alloys. The strain-hardening rate and exponent were calculated from the results, showing a large deviation from typical behavior and significant grain size dependence.

5.2. Introduction

High-entropy alloys (HEAs) have recently attracted attention as a new paradigm in alloy development. Traditional alloys are usually based on one primary element, with additional elements added to affect specific properties. HEAs however, contain several elements in high proportions, with the goal of producing a stable solid solution, thus having high mixing entropy[2]. The common definition for an HEA is an alloy with five or more elements in concentrations from 5 – 35 at%. As HEAs have no “base” element, the properties of the resultant alloy can be unexpected and difficult to predict[3]. While it was initially supposed that the high mixing entropy would be a major factor in stabilizing the solid solution for alloys of this type, it has been more recently found that enthalpy and atomic size differences are still significant, further increasing the difficulty of developing such alloys[27]. Some recent works have also shown that the formation of intermetallics can be controlled in some alloys as a strengthening mechanism[119].

Since its initial description by Cantor et al. in 2004[1], NiFeCrCoMn and similar alloys have been among the most widely studied multi-component solid solution, or “high entropy”, alloys. Previous studies of the mechanical properties of this alloy have focused on temperature effects in the equiatomic alloy[13] or alloys that are far from the equiatomic condition[120]. NiFeCrCoMn is already known to have good mechanical properties. Additionally, both its tensile strength and ductility increase at cryogenic temperatures, as deformation-induced twinning becomes a more prominent deformation mechanism[13]. This

suggests that it has a moderate stacking fault energy (SFE), which agrees with XRD-based measurements of the SFE[18].

Generally, in low-SFE materials, dislocation cross-slip and climb is impeded, as dissociation into partial dislocations with a wide spacing is more energetically favorable. They are more likely to deform by twinning. These effects increase the dislocation storage capacity, increase strain-hardening through the “dynamic Hall-Petch” effect of the deformation twins and result in an increase to both strength and ductility[54,57,58,80,81]. Subramanya Sarma et al.[121] describe the change in deformation mechanisms in Cu-Al alloys as a function of temperature and SFE. As the Al content increases (and the SFE decreases), twinning becomes the predominant deformation mechanism, with a lower SFE required for deformation twinning at room temperature deformation than is required at cryogenic temperatures[121].

In addition to copper alloys, reducing the SFE has also been found to induce twinning and increase strength in Mg-based alloys[85]. This behavior is also exploited in austenitic steel alloys to produce twinning-induced plasticity (TWIP) steels, which have high strength and good ductility[122].

In this study, we describe the results of room temperature tensile tests of non-equiatomc NiFeCrCoMn alloys optimized for low SFE. This includes the low-SFE alloy described in [18] as well as an additional alloy with an increased cobalt content[123]. For comparison, tests are also conducted on equiatomc NiFeCrCoMn and NiFeCrCo. Table 5.1 lists the nominal compositions, stacking fault energies[18,123], thermodynamic data[33], and

average atomic size difference (δ)[39,124] for the alloys used in this study. As a convention, numbers in subscripts are compositions in at%, and alloys specified without subscripts are equiatomic.

Table 5.1: Alloys used in the study, their stacking fault energies[18,123], enthalpy[33] and entropy of mixing, and RMS-deviation from average atomic size (δ)[3,39].

Alloy/Composition	γ (mJ m⁻²)	ΔH_{mix} (kJ mol⁻¹)	ΔS_{mix} (J mol⁻¹ K⁻¹)	$\delta \times 100$
NiFeCrCo	26.8	-2.45	11.52	1.181
NiFeCrCoMn	19.0	-3.04	13.37	1.057
Ni ₁₄ Fe ₂₀ Cr ₂₆ Co ₂₀ Mn ₂₀	3.5	-2.60	13.22	1.046
Ni _{18.5} Fe _{18.5} Cr _{18.5} Co ₂₆ Mn _{18.5}	9.7	-2.77	13.29	1.045

5.3. Experimental procedure

Bulk samples were prepared by arc melting pure metals (>99%) on a water-cooled copper hearth in a Ti-gettered argon atmosphere. Samples were flipped and remelted at least 3 times before being drop cast into a water-cooled 7 mm diameter cylindrical copper mold. Chemical analysis was performed using a Hitachi S3200N SEM equipped with an Oxford EDS detector to verify that all elements were within ± 1 at% of the intended composition. Sections 2 – 3 mm thick were cut from the cylinders using a low-speed diamond saw. Samples were then homogenized at 1000 °C for 24 hours in an Ar-2% H₂ atmosphere and cooled in the furnace. The homogenized samples were then cold-rolled to ~80% reduction with the rolling direction changed between passes to obtain more equal final dimensions.

In order to determine an optimal recrystallization temperature for each alloy, small samples of the rolled material were annealed for 1 h at temperatures 575 – 1100 °C. The samples were then polished and tested with a microhardness tester at a 50 g load using 10 indents per sample. X-ray diffraction analysis to check for intermetallics or phase separation was done using a Rigaku SmartLab with a Cu K α source at 40 kV and 44 mA.

Tensile samples were produced by annealing rolled sheets at medium temperatures near the recrystallization temperature (625-675 °C, depending on the sample) and at high temperature (1100 °C). “Dog bone” samples with thickness of 0.2 – 0.4 mm, gage length of ~2.5 mm, and gage width of ~1 mm were cut from the sheets using a miniature CNC mill and were polished using SiC paper and Al₂O₃ suspension. The thickness of each sample was measured using a digital micrometer and the length and width of the gage section were measured with the ImageJ software[125] from optical microscope images of each sample with a calibration slide. Tensile tests were done using a micro-tensile tester at a strain rate of $7.3 \times 10^{-4} \text{ s}^{-1}$. Analysis of the stress-strain data was done using Origin 9.0 (OriginLab, Northampton, MA) and Microsoft Excel 2010. SEM analysis of the fracture surfaces and gage surfaces was done using the aforementioned SEM. Atomic force microscopy (AFM) analysis of gage surfaces was done using a Bruker Dimension 3000 in intermittent contact (tapping) mode and MikroMasch RiteProbe TSP1 tip. Samples were cleaned with acetone and methanol prior to AFM measurements. Grain size measurements were done using the line-intercept method on optical micrographs of samples etched in a solution of 2.5 g CuCl₂, 50 mL ethanol, and 50 mL HCl.

5.4. Results and discussion

5.4.1. Recrystallization and grain growth behavior

Figure 5.1 shows the hardness vs. annealing temperature and homologous temperature (based on the solidus temperature reported in [50] for equiatomic NiFeCrCoMn) for all of the alloys. The $\text{Ni}_{14}\text{Fe}_{20}\text{Cr}_{26}\text{Co}_{20}\text{Mn}_{20}$ alloy appears to retain its as-rolled hardness up to 700 °C, but XRD analysis of the annealed material showed that this was a result of the formation of σ -phase intermetallics. However, the $\text{Ni}_{14}\text{Fe}_{20}\text{Cr}_{26}\text{Co}_{20}\text{Mn}_{20}$ sample annealed at 1100 °C did not contain any measurable amount of σ -phase, nor was it observed in any other samples. Development of σ -phase in $\text{Ni}_{14}\text{Fe}_{20}\text{Cr}_{26}\text{Co}_{20}\text{Mn}_{20}$ is consistent with the empirical predictions made in [126], that Cr-containing HEAs with a valence electron concentration (VEC) between 6.88 and 7.84 are prone to σ formation. Its average VEC is 7.76, in contrast to all of the other alloys studied which have $\text{VEC} \geq 8$. SEM observations did show the presence of manganese and chromium oxide particles in all of the Mn-containing samples, but no oxide peaks are seen in the XRD spectra, confirming that they are present in a very low volume fraction, consistent with results seen in other studies[24] where they were assumed to have no effect on the mechanical properties.

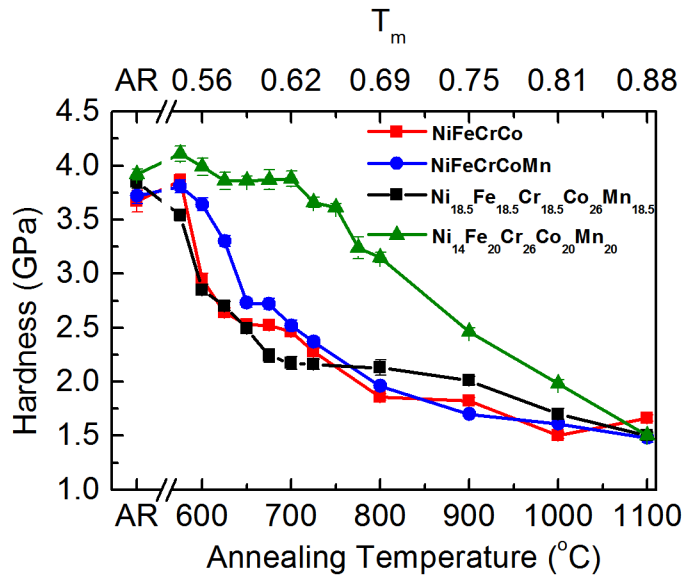


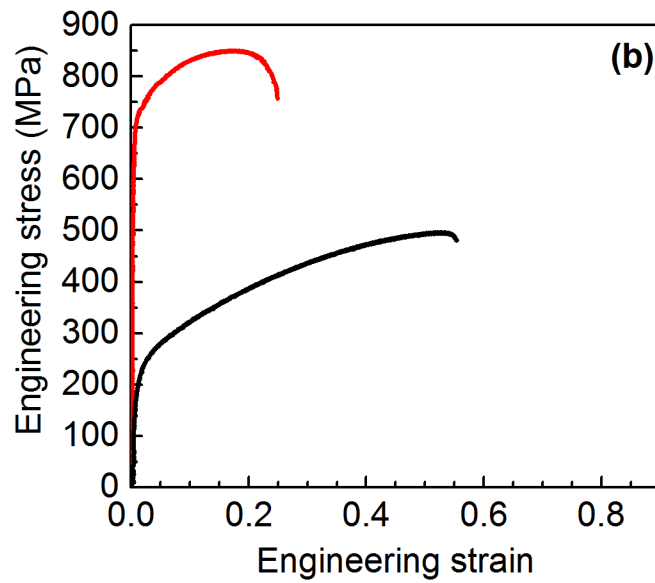
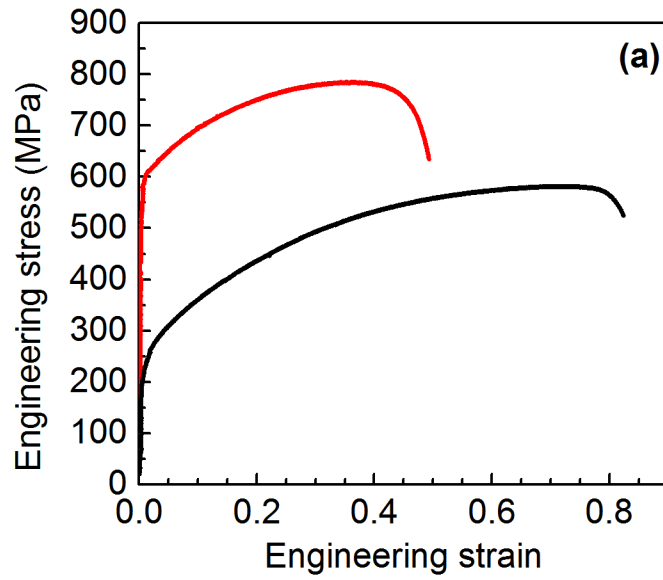
Figure 5.1: Hardness vs annealing temperature after ~80% rolling reduction (AR = as-rolled)

In the other samples, the as-rolled hardness is nearly the same and they follow similar trends, particularly at high temperatures, with NiFeCrCoMn having a slightly higher recrystallization temperature than the other alloys. For the tensile test samples, to compare alloys at similar stages of recrystallization, different temperatures were chosen using Figure 5.1 to anneal the medium-temperature samples. The recrystallization temperatures chosen for the tensile samples were: 625 °C for NiFeCrCo and Ni_{18.5}Fe_{18.5}Cr_{18.5}Co₂₆Mn_{18.5}, 650 °C for NiFeCrCoMn, and 675 °C for Ni₁₄Fe₂₀Cr₂₆Co₂₀Mn₂₀. A higher temperature was used for the latter sample to ensure complete recrystallization. All samples were annealed for 1 hour. The grain sizes of the moderate temperature-annealed samples were found to be ~1-2 μm and the 1100 °C-annealed samples were 60-80 μm.

5.4.2. Tensile tests

Representative engineering stress-strain curves for all of the samples are shown in Figure 5.2. As expected from the hardness measurements and the known presence of intermetallics, $\text{Ni}_{14}\text{Fe}_{20}\text{Cr}_{26}\text{Co}_{20}\text{Mn}_{20}$ annealed at 675 °C has a very high strength, but negligible ductility. Unexpectedly, reducing the stacking fault energy in that alloy did not result in an improvement in the mechanical properties. After annealing at 1100 °C, $\text{Ni}_{14}\text{Fe}_{20}\text{Cr}_{26}\text{Co}_{20}\text{Mn}_{20}$ performed similarly to the equiatomic alloy, but with 7% and 13% lower tensile strength and toughness, respectively. $\text{Ni}_{18.5}\text{Fe}_{18.5}\text{Cr}_{18.5}\text{Co}_{26}\text{Mn}_{18.5}$ had a higher ductility than the other 5-component alloys, but at the expense of a reduction in strength. The highest strength alloy that was still ductile was the equiatomic alloy annealed at 650 °C.

Figure 5.2: Representative tensile stress-strain curves for (a) NiFeCrCo (625 °C and 1100 °C), (b) NiFeCrCoMn (650 °C and 1100 °C), (c) Ni_{18.5}Fe_{18.5}Cr_{18.5}Co₂₆Mn_{18.5} (625 °C and 1100 °C), and (d) Ni₁₄Fe₂₀Cr₂₆Co₂₀Mn₂₀ (675 °C and 1100 °C). Red lines – moderate temperature anneal, black lines – high temperature anneal.



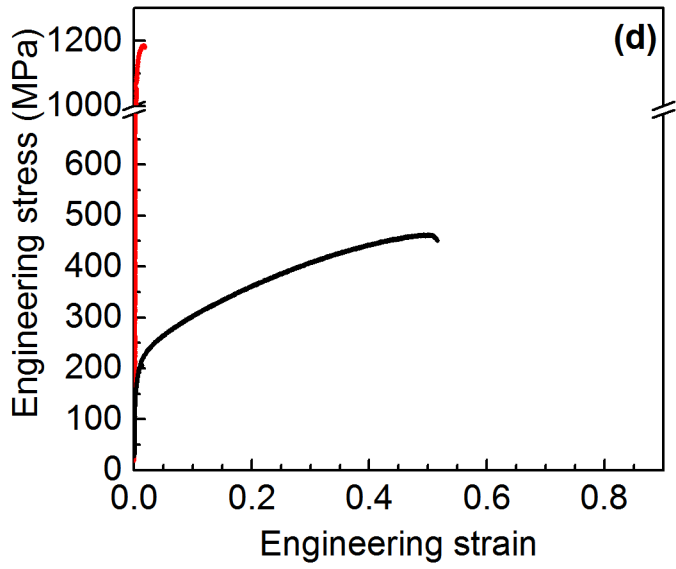
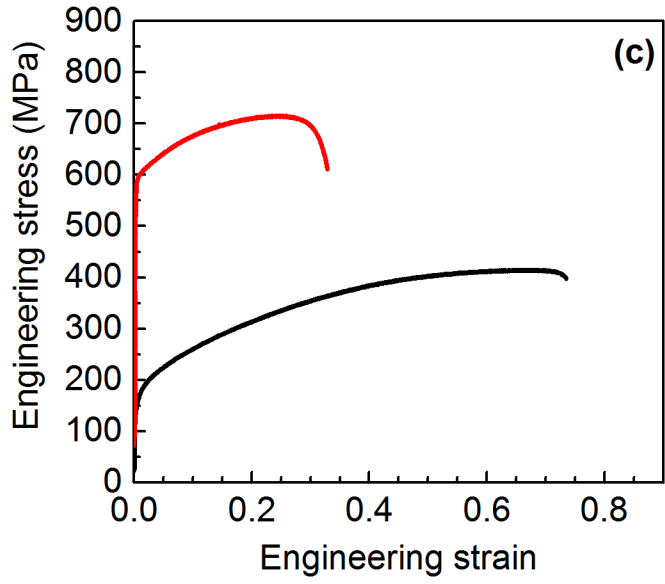


Table 5.2 shows the quantitative measurements from the tensile tests: 0.2% offset yield stress, tensile strength, total plastic elongation, uniform elongation, and toughness (defined as the area under the curve). For both the medium and high temperature-annealed samples, the toughest sample by a significant margin was the equiatomic 4-component alloy. It has a yield strength comparable to the $\text{Ni}_{18.5}\text{Fe}_{18.5}\text{Cr}_{18.5}\text{Co}_{26}\text{Mn}_{18.5}$ alloys, but with significantly higher ductility and tensile strength. Additionally, the alloys are compared to three low-stacking fault energy twinning-induced plasticity (TWIP) steels reported in [127]. The grain size of the TWIP steels was not reported and, based on the reported strength, likely falls between the grain sizes tested in this study. Nevertheless, NiFeCrCo and $\text{Ni}_{18.5}\text{Fe}_{18.5}\text{Cr}_{18.5}\text{Co}_{26}\text{Mn}_{18.5}$ appear to perform comparably to the TWIP steels, suggesting a possible use as energy absorbing materials for transportation applications.

Table 5.2: Numerical results of tensile tests: yield stress, tensile stress, percent elongation, uniform elongation, and tensile toughness (calculated as the integral of the engineering stress-strain curve). Values for three TWIP steels are included for comparison[127].

Annealing Temperature (°C)	Alloy	σ_y (MPa)	σ_{UTS} (MPa)	%EL	Uniform %EL	Toughness (J cm ⁻³)
1100	Ni _{18.5} Fe _{18.5} Cr _{18.5} Co ₂₆ Mn _{18.5}	134	414	73.5%	66.5%	257
1100	Ni ₁₄ Fe ₂₀ Cr ₂₆ Co ₂₀ Mn ₂₀	162	462	51.6%	50.1%	193
1100	NiFeCrCoMn	135	497	55.4%	53.5%	224
1100	NiFeCrCo	197	582	82.4%	70.3%	408
625	Ni _{18.5} Fe _{18.5} Cr _{18.5} Co ₂₆ Mn _{18.5}	586	715	32.8%	24.3%	223
675	Ni ₁₄ Fe ₂₀ Cr ₂₆ Co ₂₀ Mn ₂₀	1153	1187	1.8%	1.7%	19.5
650	NiFeCrCoMn	660	851	24.9%	17.4%	201
625	NiFeCrCo	540	786	49.3%	35.4%	360
	Fe _{70.04} Mn ₂₈ Al _{1.6} Si _{0.28} C _{0.08}	325	495	64%	48%	
	Fe _{73.03} Mn ₂₅ Al _{1.6} Si _{0.24} Nb _{0.05} C _{0.08}	375.5	538	61%	50%	
	Fe _{68.25} Mn ₂₇ Al _{4.1} Si _{0.52} Nb _{0.05} C _{0.08}	383	548	61%	38%	

In single-phase alloys such as these, it is expected that solid solution strengthening has a major role in the mechanical properties. The effects of this can be observed in the results of the coarse-grained samples. For the contribution from solid solution strengthening, the stress required to move a dislocation is affected by both lattice distortion and shear modulus differences [54,62]. From the values of δ in Table 5.1, it can be seen that the lattice distortion in these alloys is relatively small and not substantially different between any of the 5-component alloys. The shear moduli of iron, nickel, cobalt, and manganese are also similar, 82 GPa, 76 GPa, 75 GPa, and 81 GPa, respectively (the shear modulus of Mn is using the Young's modulus, bulk modulus, and isotropic elastic constant relationships). The shear modulus of chromium however is much higher, 115 GPa [128]. Indeed, the alloys with the highest Cr content, NiFeCrCo (25%) and Ni₁₄Fe₂₀Cr₂₆Co₂₀Mn₂₀ have the highest yield strengths of the coarse-grained samples. In the fine-grain samples, Hall-Petch strengthening likely plays a more dominant role.

Figure 5.3 shows the fracture surfaces of the NiFeCrCo (a) and NiFeCrCoMn (b) 1100 °C samples. While both show the typical dimpled appearance of a ductile fracture surface, there is a substantial difference in the appearance of the two fracture surfaces. The surface of NiFeCrCo contains numerous small dimples, < 2 μm . In contrast, the NiFeCrCoMn contains mostly large dimples with small particles visible inside. EDS analysis shows that these are the Mn-Cr oxide particles common to most cast NiFeCrCoMn-alloy systems. The fracture surfaces of all of the Mn-containing alloys showed a similar appearance. This suggests that while the oxide particles do not affect the yield strength of the

alloys, they do have a deleterious effect on the ductility and toughness as preferred nucleation sites for microvoids [129]. As NiFeCrCo does not contain any second phase particles, microvoid nucleation likely occurs on smaller defects, requiring a larger critical stress [130].

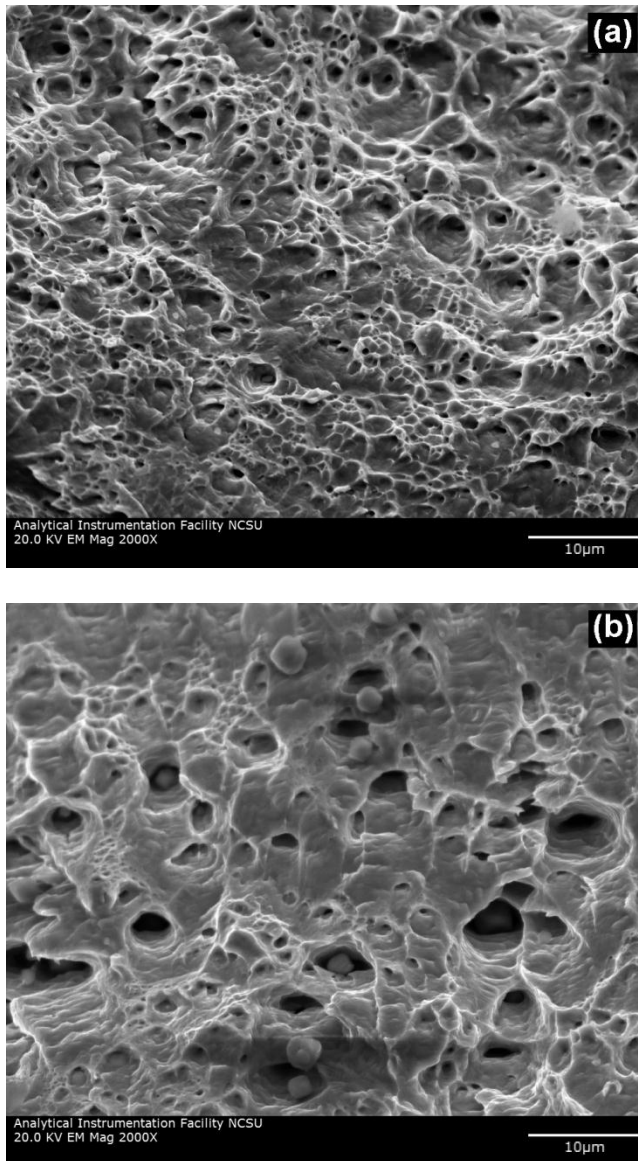


Figure 5.3: Secondary electron images of the fracture surfaces of (a) NiFeCrCo and (b) NiFeCrCoMn.

A significant effect on the gage surfaces of the samples was also observed after testing. The samples were polished prior to testing, but underwent significant roughening or wrinkling during the tests indicating substantial out-of-plane and localized deformation. The

effect is most noticeable on the coarse-grained samples but it does also affect the finer-grained samples. Both samples of $\text{Ni}_{18.5}\text{Fe}_{18.5}\text{Cr}_{18.5}\text{Co}_{26}\text{Mn}_{18.5}$ are shown in Figure 5.4. The RMS roughness of the 625 °C-annealed sample is 114 nm and the total variation between the lowest and highest points is ~800 nm, on a similar order as the grain size. As the relatively low stacking fault energy of the alloys impedes cross-slip and climb, mechanisms involving high localized and grain-scale deformation reorient the crystal to maximize shear stress along preferred slip systems to enable dislocation glide [131,132]. The effect in the coarse-grained was likely exacerbated by the low thickness of the sample, which was only a small multiple of the grain size; therefore, it may deviate from conventional polycrystal behavior.

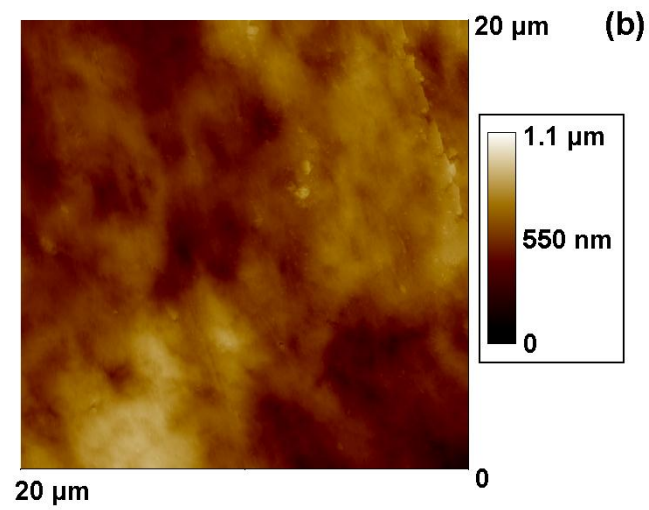
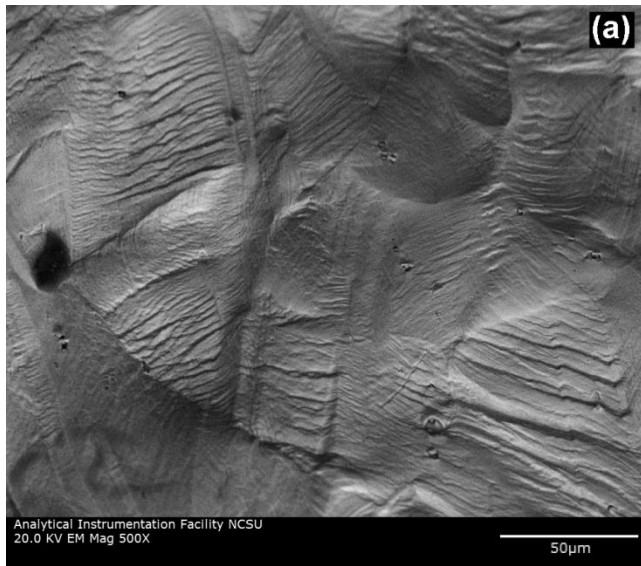


Figure 5.4: Gage surfaces of $\text{Ni}_{18.5}\text{Fe}_{18.5}\text{Cr}_{18.5}\text{Co}_{26}\text{Mn}_{18.5}$ after testing. (a) Backscattered electron image of 1100 °C sample. (b) AFM image of 625 °C sample.

5.4.3. Strain-hardening behavior

There are several common methods used to measure strain-hardening from tensile test data using the true stress and true strain during plastic deformation up to the point of necking. The most common method[54] uses the equation:

$$\sigma = K\varepsilon^n \quad (5.1)$$

where K is the strength coefficient and n is the strain-hardening exponent. The values can be calculated using a linear fit to the true stress-true strain curve on a log-log plot. Using this method, one obtains rather low values for n for the HEAs tested here, 0.12 – 0.18 for the medium temperature-annealed samples (excluding $\text{Ni}_{14}\text{Fe}_{20}\text{Cr}_{26}\text{Co}_{20}\text{Mn}_{20}$, for which the plastic deformation was too short for a reasonable fit). However, the log-log true strain data is not very linear, resulting in R^2 coefficients of determination for linear fits of 0.92 – 0.97.

Another method[54] uses a similar equation:

$$\sigma = \sigma_0 + K\varepsilon^n \quad (5.2)$$

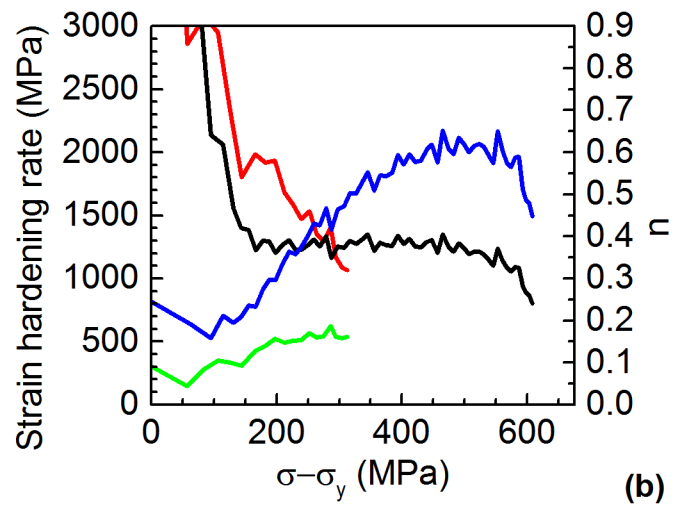
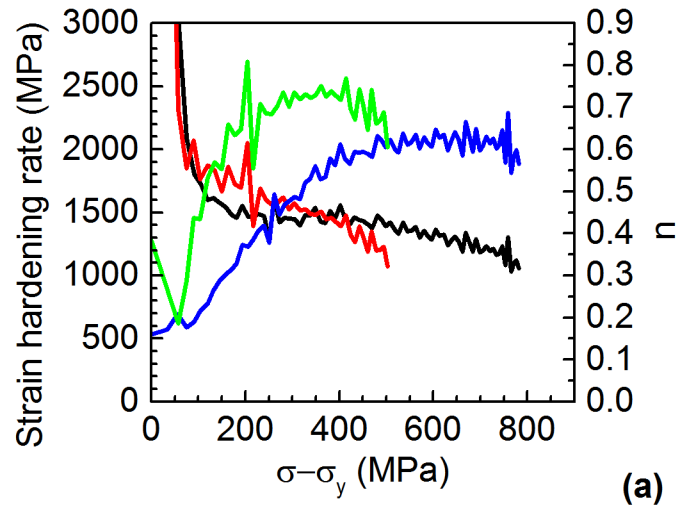
where σ_0 is the yield stress. Using a fit of this type, R^2 is improved to better than 0.998 for the finer-grained sample results. However, this method still results in a poor fit to the high temperature-annealed sample data, particularly at low strain values, at which the residuals are as high as 35 MPa.

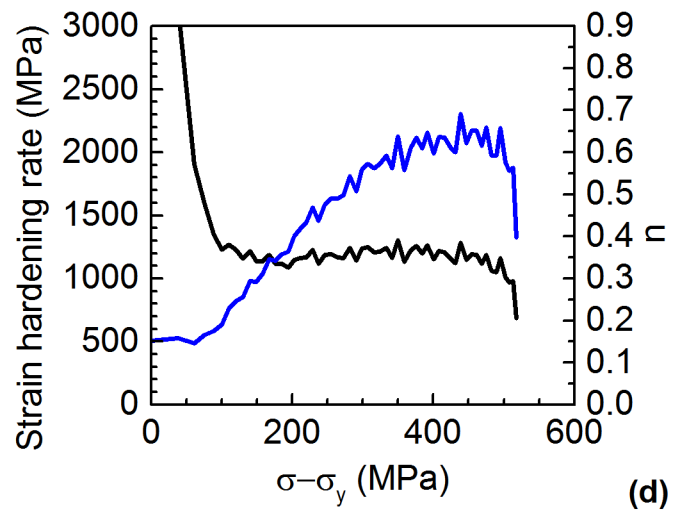
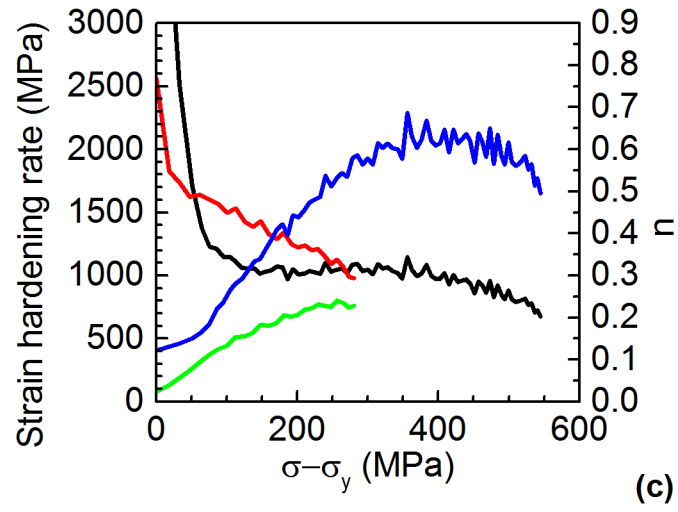
The strain-hardening exponent at any given point on the stress-strain curve can also be derived from the strain-hardening rate[54,122]:

$$n = \frac{d\sigma}{d\varepsilon} \frac{\varepsilon}{\sigma} \quad (5.3)$$

Plots showing the strain-hardening rate and exponent calculated using equation 5.3 as a function of true stress are shown in Figure 5.5. To produce these, the original data was smoothed to reduce the random electronic noise between points using an adjacent-averaging method and increasing the distance between points. Some noise is still present, visible as the slight oscillations between points at high stress.

Figure 5.5: Strain-hardening rate (left axis) and exponent (right axis) as a function of true stress subtracted by yield stress for (a) NiFeCrCo, (b) NiFeCrCoMn, (c) Ni_{18.5}Fe_{18.5}Cr_{18.5}Co₂₆Mn_{18.5}, and (d) Ni₁₄Fe₂₀Cr₂₆Co₂₀Mn₂₀ (1100 °C only). Color key: Black: coarse-grain strain-hardening rate. Blue: coarse-grain exponent. Red: fine-grain rate. Green: fine-grain exponent.





An interesting trend can be observed in the results. For most of the alloys, the strain-hardening behavior is dependent on the grain size. The coarse-grained samples annealed at 1100 °C all follow a nearly identical trend independent of the composition, in which the exponent gradually increases, then remains constant at around ~0.6. The strain-hardening rate rapidly drops up to ~100 MPa, and then remains nearly constant. In the finer-grained samples annealed at lower temperatures, there is a substantial difference; the strain-hardening rate continuously decreases with increasing stress, leading to a much lower exponent, with the equiatomic NiFeCrCoMn being the lowest. The exception to this is the 4-component equiatomic alloy, in which the fine-grain sample behaves more similar to the coarse-grain sample, with a strain-hardening exponent ~0.7. This difference is apparent when comparing NiFeCrCo to Ni_{18.5}Fe_{18.5}Cr_{18.5}Co₂₆Mn_{18.5} annealed at 625 °C. The yield stress of the Co-rich alloy is 46 MPa larger, but at 24.3% strain, the stress on the NiFeCrCo sample is 50 MPa larger. This rapid strain-hardening contributes significantly to the toughness of NiFeCrCo, allowing it to outperform the substantially stronger NiFeCrCoMn by almost 80%.

The strain-hardening rate is also comparable to, if not higher than, that of the previously discussed TWIP steels. In the flat portion of the strain-hardening curve, the TWIP steels harden at a rate of 800 – 1200 MPa[127] while the alloys reported in this study harden at a rate of 1000 – 1500 MPa.

5.4.4. Effect of stacking fault energy

Reducing the stacking fault energy did not have as large of an effect on strength and ductility as was expected. At 1100 °C, the yield strength of $\text{Ni}_{14}\text{Fe}_{20}\text{Cr}_{26}\text{Co}_{20}\text{Mn}_{20}$ was slightly improved over the equiatomic alloy, but ductility was poorer. The increased Cr content may have increased the number of oxide particles. In addition, the alloy exhibited poor thermal stability, forming σ -phase particles after annealing at temperatures <1100 °C preventing assessment of the strength and ductility of the fcc matrix with a fine grain structure. $\text{Ni}_{18.5}\text{Fe}_{18.5}\text{Cr}_{18.5}\text{Co}_{26}\text{Mn}_{18.5}$ exhibited higher ductility than the equiatomic 5-component alloy, but a lower strength after the moderate-temperature anneal, even when using a lower recrystallization temperature than the equiatomic alloy. The high-Co alloy did however have a 10-15% greater toughness compared to NiFeCrCoMn at both annealing temperatures.

In the case of NiFeCrCo, it is difficult to say whether the improvement is a result of the SFE (which is expected to be similar to, if not higher than, NiFeCrCoMn) or the lack of oxide particles. The higher ductility and strain-hardening rate compared to the other alloys suggest that a low SFE and deformation twinning are factors in the mechanical properties. The higher coarse-grain yield strength compared to NiFeCrCoMn may be a result of the lower SFE, or, as discussed earlier, a result of solid solution strengthening due to the higher Cr content.

A prior study did not observe any deformation twinning in equiatomic NiFeCrCoMn during room temperature tensile tests [13]. However, another study using rolling rather than

tensile testing did find evidence of deformation twinning at room temperature [133].

Therefore, the presence of twinning, especially at extremely high strains cannot be ruled out entirely. In similar materials that show significant deformation by twinning, such as TWIP steels, it is known that twin nucleation and other deformation mechanisms that affect strain-hardening behavior are grain size-dependent [122]. A similar trend is observed here in the NiFeCrCoMn and $\text{Ni}_{18.5}\text{Fe}_{18.5}\text{Cr}_{18.5}\text{Co}_{26}\text{Mn}_{18.5}$ results in which, after the initial decrease, the strain-hardening rate is larger in the finer grained samples. Further research is needed to determine the deformation mechanisms in NiFeCrCo and $\text{Ni}_{18.5}\text{Fe}_{18.5}\text{Cr}_{18.5}\text{Co}_{26}\text{Mn}_{18.5}$.

5.5. Conclusion

Low-stacking fault energy NiFeCrCoMn-based high entropy alloys were produced by arc melting, rolling, and recrystallization. Tensile tests were conducted in order to characterize their mechanical properties as a function of grain size and composition.

All of the alloys exhibited similar recrystallization and grain growth behavior after ~80% rolling reduction, with recrystallization temperatures 625-675 °C.

$\text{Ni}_{14}\text{Fe}_{20}\text{Cr}_{26}\text{Co}_{20}\text{Mn}_{20}$ exhibited poor thermal stability, forming σ -phase particles when annealed below 1100 °C. All other samples remained single-phase fcc, except for a small (undetectable by x-ray diffraction) volume fraction of manganese-containing oxide particles in all alloys except NiFeCrCo.

NiFeCrCo exhibited the best combination of strength and ductility in both coarse grain and fine grain conditions, with yield strength of nearly 200 MPa and uniform

elongation of 70% after annealing at 1100 °C, and 80% higher toughness than NiFeCrCoMn after the same processing conditions. $\text{Ni}_{18.5}\text{Fe}_{18.5}\text{Cr}_{18.5}\text{Co}_{26}\text{Mn}_{18.5}$, which adds additional cobalt to the base alloy to reduce the SFE had a 30% improvement in elongation compared to the equiatomic alloy, but at the expense of an 11% reduction in yield strength in the fine-grain condition. The reduced ductility of all of the Mn-containing samples compared to NiFeCrCo is attributed to the oxide particles, which act as preferred nucleation sites for microvoids.

The strain-hardening behavior of the alloys was characterized using the strain-hardening rate and exponent as a function of stress. Strain-hardening shows a strong grain size dependence, with fine-grain samples having a much lower strain-hardening exponent and continuously decreasing strain-hardening rate. Coarse-grain samples have a high strain-hardening exponent and nearly constant strain-hardening rate (after an initial decrease). The exception to this is NiFeCrCo, which has a high exponent and constant rate regardless of the grain size, contributing to its high toughness. The alloys perform comparably to twinning-induced plasticity steels in terms of ductility and strain-hardening, suggesting a possible application as energy-absorbing materials.

6. SINGLE CRYSTAL ELASTIC CONSTANTS OF EQUIATOMIC NiFeCrCoMn DETERMINED BY NANOINDENTATION

6.1. Abstract

The single crystal stiffness constants of NiFeCrCoMn were determined by nanoindentation. $C_{11} = 215$ GPa, $C_{12} = 107$ GPa, and $C_{44} = 103$ GPa. These values are reasonably consistent with those calculated by *ab initio* methods. The recalculated stacking fault energy from the measured values is also consistent with the SFE determined using calculated values as well as experimental observations of the deformation mechanisms at different temperatures.

6.2. Introduction

Significant attention has been paid to the deformation mechanisms of solid solution alloys containing multiple principal elements, commonly called high-entropy alloys (HEAs). Because they are single-phase materials, their strength must come from solid-solution strengthening [134], grain size strengthening [9,135], and other mechanisms of impeding dislocation motion through lattice-scale effects, such as reducing the stacking fault energy (SFE) [18]. NiFeCrCoMn has attracted particular attention due to its relatively high strength and high ductility, both of which increase at low temperatures [13,24]. Detailed studies of its deformation mechanisms have shown that it deforms by twinning at cryogenic temperature [13] and, at least in some cases, at room temperature as well [133]. This is consistent with an alloy having a medium to low SFE [24]. Indeed, measurements of the SFE of the alloy have

shown it to be 20-27 mJ m⁻². These measurements however, rely on elastic constants calculated using first-principles modelling, which has proven difficult with such complex alloys [3,52].

Knowing the single crystal elastic constants is necessary for any further detailed studies of stacking faults in the alloy. In addition to the x-ray diffraction-based technique described by Reed and Schramm[73], the elastic constants are also needed for accurate determination in conventional electron microscopy-based techniques that measure the separation between partial dislocations, to determine the shear modulus and Poisson's ratio in the direction of the dislocation [59,136]. Additionally, the elastic constants are useful for other analyses involving dislocations and other defects,[115,137,138] the elastic properties of textured materials,[139] atomic bonding and interactions, and phonon properties such as the Debye temperature [115,140].

To date, only the polycrystalline elastic constants of NiFeCrCoMn have been experimentally determined [48]. Producing bulk single crystals of high-entropy alloys is also challenging, and few such results have been reported [46]. However, Pierce et al. developed a technique for a similar material (twinning-induced plasticity steel), in which nanoindentation is used to measure the single crystal properties of a polycrystalline material, which can then be related back to the single crystal elastic constants. On tests of metals with known single crystal elastic constants (Al, Cu, W, 316L steel, and β -brass) the nanoindentation-measured values were within 10% of literature values determined by conventional methods [60]. Here that method is applied to the equiatomic high-entropy alloy, NiFeCrCoMn.

6.3. Experimental procedure

A sample of equimolar NiFeCrCoMn was prepared by arc melting pure metals (>99%) on a water-cooled copper hearth in a Ti-gettered argon atmosphere. The sample was flipped and remelted 3 times before being drop cast into a water-cooled cylindrical 7 mm diameter copper mold. The cylinder was cut into sections using a low-speed diamond saw and a section of the cast cylinder was homogenized at 1000 °C for 24 hours in an Ar-2% H_2 atmosphere, then cold-rolled to approximately 300 μm thickness and annealed again for 2 hours at 1000 °C. Specimens were cut from the sheet using a miniature CNC mill, polished with SiC papers up to 1200 grit, and then given a final polish with 0.05 μm alumina slurry using a vibratory polisher. Finally, the samples were lightly etched in a solution of 2.5 g CuCl_2 , 50 mL ethanol, and 50 mL HCl.

Electron backscatter diffraction (EBSD) maps, such as the one in Figure 6.1 were produced of multiple regions on a specimen using an FEI Quanta 3D FEG with an Oxford Nordlys detector. The microscope's focused ion beam was used to mill patterns in the center of the sample to provide reference points for the nanoindenter's optical microscope and for drift correction by observing how far the milled pattern moved in electron images taken before and after mapping. The Oxford Channel5 software was used to identify grains in each region near $\{100\}$ and $\{111\}$ and their x, y coordinates relative to a reference point on the pattern were measured using ImageJ.

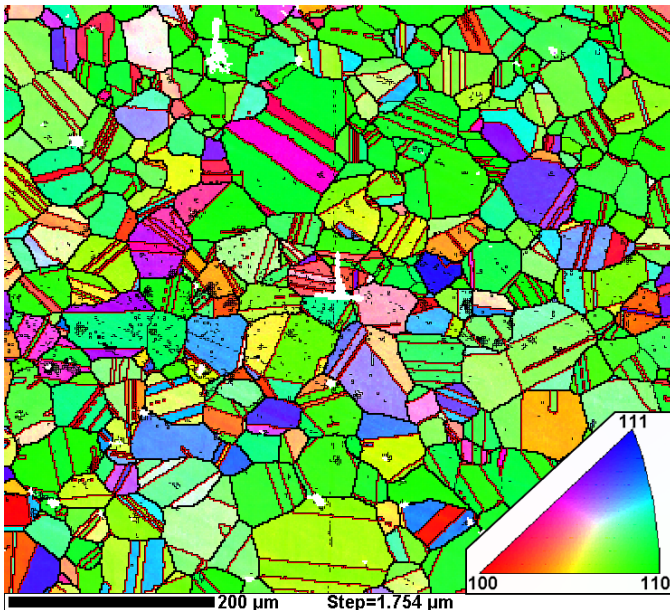


Figure 6.1: EBSD map of NiFeCrCoMn. The reference pattern is visible as a white (unindexed) region near the center.

Nanoindentation measurements were taken using a Hysitron Triboindenter with a 100 nm radius Berkovich tip operated in load-controlled mode. The area function of the tip was calibrated using a material of known modulus (fused quartz). A $10\ \mu\text{m} \times 10\ \mu\text{m}$ grid of 20 indents was made around the center of each grain. A maximum load of $1500\ \mu\text{N}$ was used, with a $250\ \mu\text{N s}^{-1}$ loading/unloading rate and 5 second hold. This resulted in a typical contact depth of approximately 100 nm. The reduced modulus was determined from the unloading curve using the Oliver-Pharr method [68]. An example load vs. depth curve for a $\{111\}$ grain is shown in Figure 6.2.

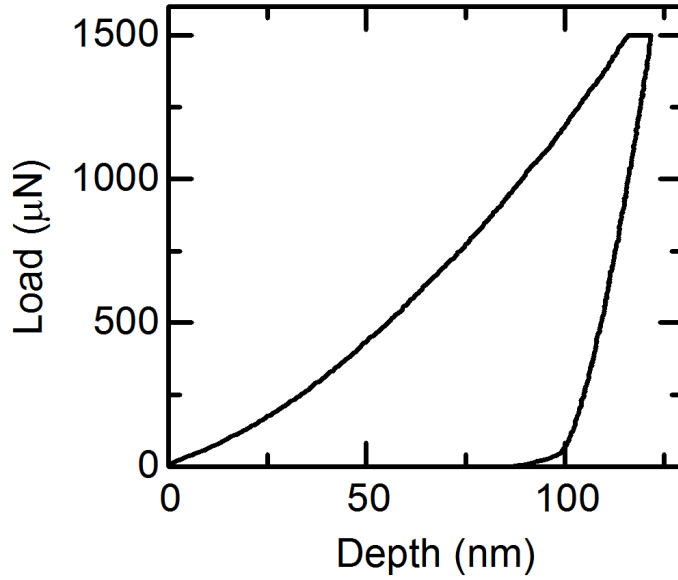


Figure 6.2: Load vs. depth curve for {111} grain.

6.4. Results and discussion

The single crystal elastic constants were measured using the method described by Pierce et al. [60]. The average reduced modulus (E_r) of each grain was calculated, after excluding indents with extremely shallow or extremely deep contact depths, likely due to surface defects or oxide particles. Grains with too many (more than 4) excluded points were not used for analysis. Then the average reduced modulus for each orientation was calculated as the average of all grains in the orientation and converted to the orientation dependent indentation modulus, M_{hkl} , using

$$\frac{1}{E_r} = \frac{1}{M_{hkl}} + \frac{1 - \nu_i^2}{E_i} \quad (6.1)$$

where E_i and ν_i are the Young's modulus and Poisson ratio of the indenter, 1140 GPa and 0.07, respectively. The single crystal elastic constants were then calculated by simultaneously solving several equations. First, the Hershey-Kröner-Eshelby (HKE) method[141] relates the polycrystalline shear modulus (G) to the stiffness constants:

$$G^3 + \alpha G^2 + \beta G + \gamma = 0 \quad (6.2)$$

where

$$\alpha = \frac{5c_{11} + 4c_{12}}{8} \quad (6.3)$$

$$\beta = -\frac{c_{44}(7c_{11} - 4c_{12})}{8} \quad (6.4)$$

$$\gamma = -\frac{c_{44}(c_{11} - c_{12})(c_{11} + 2c_{12})}{8} \quad (6.5)$$

The Vlassak-Nix model[142] relates M_{hkl} to the polycrystalline indentation modulus with an orientation-dependent correction factor:

$$M_{hkl} = \beta_{hkl} \left(\frac{E}{1 - \nu^2} \right) \quad (6.6)$$

where β_{hkl} is given by

$$\beta_{hkl} = a + c(A - A_0)^B \quad (6.7)$$

a , c , A_0 , and B depend on the orientation and $\nu_{\langle 100 \rangle}$, the Poisson ratio in the $\langle 100 \rangle$ direction, given by $c_{12}/(c_{11} + c_{12})$ and were determined using a polynomial extrapolation of the values given in [142]. This model is solved for A , the anisotropy ratio, $2c_{44}/(c_{11} - c_{12})$ using

$$\frac{M_{111}}{M_{100}} = \frac{a_{111} + c_{111}(A - A_{0,111})}{a_{100} + c_{100}(A - A_{0,100})} \quad (6.8)$$

Finally, the polycrystalline and single crystal bulk moduli are assumed to be equal:

$$K = \frac{E}{3(1 - 2\nu)} = \frac{c_{11} + 2c_{12}}{3} \quad (6.9)$$

The polycrystalline Young's modulus and Poisson ratio of NiFeCrCoMn at 300 K determined by resonant ultrasound spectroscopy in [48] were used, 202 GPa and 0.265, respectively. Using those values, M_{100} , and M_{111} , equations 6.2, 6.8, and 6.9 were simultaneously solved for the single crystal elastic constants using the Levenberg–Marquardt least-squares algorithm implemented in the Scipy library[143] (version 0.15.1) for Python (version 3.4.2). The code for these calculations is provided in the appendix.

The measured nanoindentation moduli and elastic constants are given in Table 6.1.

Table 6.1: Measured indentation moduli, polycrystalline elastic properties, and single crystal elastic constants of NiFeCrCoMn

M_{100} (GPa)	M_{111} (GPa)	E (GPa)	ν	C_{11} (GPa)	C_{12} (GPa)	C_{44} (GPa)
158	171	202	0.265	215	107	103

These values are reasonably consistent with previously published values calculated by density functional theory, showing a similar magnitude and the same trend ($C_{11} > C_{12} > C_{44}$) [18]. With the previously calculated values and x-ray diffraction-based stacking fault probability measurements, the stacking fault energy of the equiatomic alloy was calculated to be between 18-25 mJ m⁻². Using the values measured in this work with the previously-

measured stacking fault probabilities, the SFE is $\sim 26 \text{ mJ m}^{-2}$. A slightly higher value is consistent with studies of the deformation mechanisms, which did not observe any deformation twinning at room temperature, but did at lower temperatures [13]. This value of the stacking fault energy is calculated entirely from measured values and does not rely on any first-principles-based calculations.

6.5. Conclusions

The single crystal elastic constants of an equiatomic NiFeCrCoMn high-entropy alloy were calculated using nanoindentation measurements of grains oriented in $\{100\}$ and $\{111\}$ in a polycrystalline sample. The measured values are consistent with those calculated using first-principles modeling. The stacking fault energy calculated using the elastic constants and previously-measured x-ray stacking fault probabilities is consistent with the observed deformation mechanisms.

7. STRUCTURE AND MAGNETIC PROPERTIES OF A MULTI-PRINCIPAL ELEMENT Ni-Fe-Cr-Co-Zn-Mn ALLOY

A version of this chapter has been submitted to *Intermetallics* by A. J. Zaddach, C. Niu, A. A. Oni, M. Fan, J. M. LeBeau, D. L. Irving, and C. C. Koch. A. Zaddach prepared the powder samples, conducted x-ray, mechanical and magnetic measurements, and did the analysis of the experimental data.

7.1. Abstract

A nanocrystalline alloy with a nominal composition of $\text{Ni}_{20}\text{Fe}_{20}\text{Cr}_{20}\text{Co}_{20}\text{Zn}_{15}\text{Mn}_5$ was produced by mechanical alloying and processed using annealing treatments between 450-600 °C for lengths from 0.5-4 hours. Analysis was conducted using x-ray diffraction, transmission electron microscopy, magnetometry, and first-principles calculations. Despite designing the alloy using empirical high-entropy alloy guidelines, it was found to precipitate numerous phases after annealing. These precipitates included a magnetic phase, $\alpha\text{-FeCo}$, which, after the optimal heat treatment conditions of 1 hour at 500 °C, resulted in an alloy with reasonably good hard magnetic properties. The effect of annealing temperature and time on the microstructure and magnetic properties are discussed, as well as the likely mechanisms that cause the microstructure development.

7.2. Introduction

Conventional alloys are generally based on a single principal element with additional elements added to affect specific properties. Even complex alloys such as Alnico[144] and Inconel[145] alloys contain no more than 2 elements in concentrations above 20%. Over the past several years, significant attention has been given to alloys containing five or more elements in equal, or nearly equal atomic ratios. Alloys of this type can be difficult to design, as phase equilibria data is often unavailable for high-concentration multi-component mixtures beyond binary systems and common ternaries. Most focus is on solid solution alloys, called “high-entropy” alloys (HEAs) due to their high configurational entropy [2]. However, limiting to solid solutions also limits the potential properties and applications, as the controlled formation of secondary phases can result in properties difficult or impossible to achieve in a single-phase material. Many engineering metals used today contain multiple phases. Therefore, some research has also been conducted on multi-principal element alloys that may not meet the strict HEA definition but have interesting properties. Several alloys have been developed with age-hardening capabilities[119,146] while others have been alloyed with non-metal elements such as boron to form phases that aid in wear-resistance and high-temperature strength [147].

To date there has been little research on the magnetic properties of HEAs or other multi-principal element alloys. The single-phase NiFeCrCo alloy has been shown to be ferromagnetic, with properties dependent on short-range chemical ordering. However, the magnetic properties of the ball-milled alloy at room temperature are poor and when produced

by casting it has a Curie temperature near 100 K [52]. A BiFeCoNiMn thin film was found to have hard magnetic behavior after annealing [22] and hard magnetic behavior has been observed in an AlCoCrCuFeNi alloy [148].

In this study, we describe a nanostructured NiFeCrCoZnMn alloy prepared by mechanical alloying. We characterize the magnetic properties and microstructure as a function of heat treatment time and temperature, and describe how the magnetic properties relate to the microstructure. Empirical HEA design guidelines predict the alloy to form a stable solid solution, but we show from experimental and first-principles computational methods that formation of a multiphase alloy is energetically preferred.

7.3. Methods

Alloy powders were prepared by mechanical alloying elemental powders in a SPEX 8000 mixer mill. Powders of at least 99% purity were loaded into a stainless steel vial in a high-purity argon atmosphere with approximately 0.7 wt% dodecane as a process control agent (PCA). A 10:1 ball-to-powder weight ratio was used, with stainless steel balls. The sample was milled at room temperature for 24 hours. Before any analysis, the sample powder was put in a vacuum chamber for 18 hours to evaporate any dodecane remaining on the surface.

Samples of ~0.09 grams were compacted into 3 mm diameter cylinders using cold uniaxial pressing. Samples were then annealed at 450, 500, 550, and 600 °C for 0.5, 1, 2, and

4 hours in an Ar-2% H_2 atmosphere. Hardness tests were conducted using a Buehler microhardness tester with a 100 g load.

X-ray diffraction (XRD) analysis was conducted on the as-milled powders as well as the samples annealed at 500 °C for 1 and 4 hours using a Rigaku SmartLab diffractometer with Cu $K\alpha$ radiation. Phase analysis was done using Pananalytical HighScore Plus software with the ICDD PDF-4+ database [149]. Further analysis for lattice parameter determination was done using the PM2K Whole Powder Pattern Modeling program [72]. Compositional analysis of the as-milled and 2 hour/500 °C samples were done using a Hitachi S3200N scanning electron microscope (SEM) equipped with an Oxford energy dispersive x-ray spectroscopy (SEM/EDS) detector, using an accelerating voltage of 30 kV.

Magnetization versus field (M vs. H) curves were measured using a Quantum Design MPMS SQUID-VSM at 1.8 K and 300 K with an applied field between ± 20 kOe.

The 1 hour/500 °C sample was prepared for transmission electron microscopy (TEM) sample using an FEI Quanta 3D FEG dual-beam focused ion beam (FIB)/SEM with the in-situ lift-out technique. Energy dispersive X-ray spectroscopy (STEM/EDS) analysis was performed using a probe-corrected FEI Titan G2 60-300 kV S/STEM equipped with an X-FEG source operated at 200 kV. Bruker Esprit was used for post-processing with a 3-pixel smoothing filter to reduce noise. Standardless quantification was performed for all EDS spectra using the Q-map function. All EDS maps were formed using X-ray K-lines.

First principles calculations were performed by the exact muffin-tin orbital method combined with coherent potential approximation (EMTO-CPA) [89]. The Perdew-Burke-

Ernzerhof version of generalized gradient approximation (GGA-PBE) of exchange-correlation functionals was used [101,102]. The Kohn-Sham equations were solved within the so-called soft-core approximation, which let the code recalculate core states after each iteration. The Green's function was calculated for 16 complex energy points. The basis set of EMTO included s, p, d, and f states. A $13 \times 13 \times 13$ k-point mesh was used; the total energy converged within 1 meV/atom. The screened impurity model parameter of 0.902 was applied for electrostatic correction to the single-site CPA. Equilibrium lattice parameters were obtained by fitting volume-energy data to the Vinet equation of state [150]. Similar calculations have proven to agree well with experiments [18,52].

7.4. Results and discussion

7.4.1. Alloy structure

The NiFeCrCoZnMn alloy forms a single-phase fcc solid solution after ball milling as shown in Figure 7.1a. The nominal composition of the alloy is Ni₂₀Fe₂₀Cr₂₀Co₂₀Zn₁₅Mn₅. SEM/EDS measurements of the as-milled alloy showed a higher Fe concentration (~23 at%) and reduced Ni and Co content, as is common with ball milling using steel media. The formation of a solid solution is predicted by the empirical HEA solid solution formation rules [27,36,151]. $\Omega = 7.18$ and $\delta = 4.31\%$. Additionally, the largest $|\Delta H_{mix}|$ value for the binary systems in the alloy using Miedema's model is only 9 kJ mol⁻¹ [33]. These values suggest that the system should form a stable solid solution.

However, after annealing at 500 °C for 1 hour, numerous additional peaks can be seen in the XRD results, shown in Figure 7.1b. Due to the complex nature of the alloy and large numbers of the elements, STEM/EDS analysis was used in conjunction with conventional automated XRD phase analysis. The presence of various phases can be observed in the EDS maps presented in Figure 7.2. Using this data, the phases in the alloy can be identified based on XRD results. Table 7.1 shows the phases identified in the 1 hour/500 °C sample, their lattice parameters, the lattice parameters of the phase reported in the PDF-4+ database [149], and the average composition of 12-21 particles from the EDS maps. Due to the high degree of peak overlap, quantitative XRD phase analysis was not attempted. The carbon in the carbide phase was likely incorporated into the powder during milling from the organic PCA. The PDF entries referred to are 04-004-6329 (NiZn), 04-003-5514 (FeCo), and 01-089-2724 (Cr_{23}C_6). No significant change in overall composition was observed by SEM/EDS after 2 hours at 500 °C.

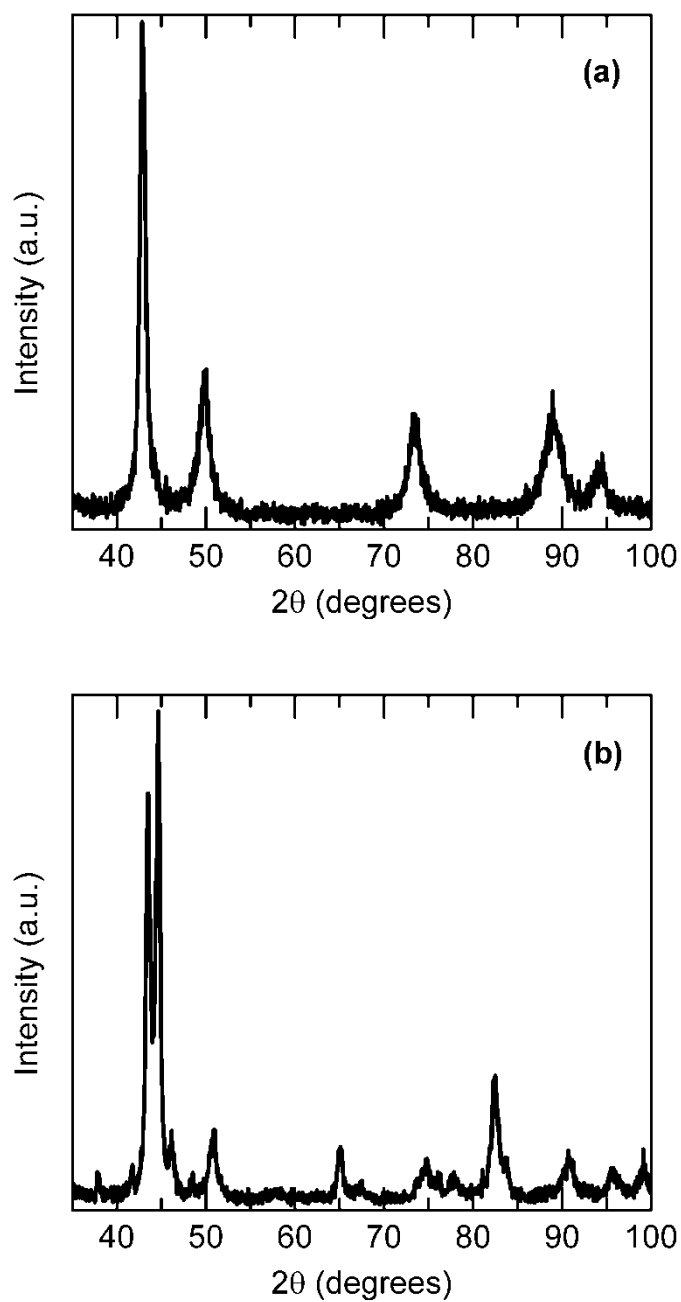


Figure 7.1: XRD pattern of (a) as-milled NiFeCrCoZnMn alloy and (b) alloy after 1 hour, 500 °C anneal.

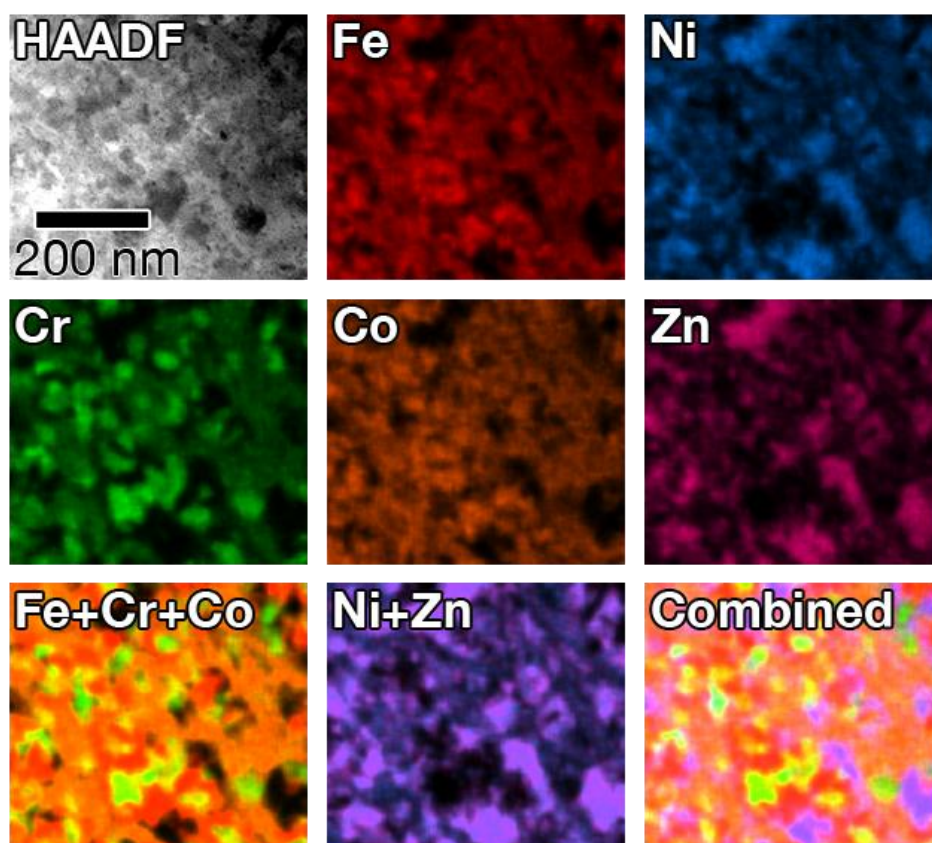


Figure 7.2: EDS maps showing the distribution and morphology of precipitate phases after 1 hour, 500 °C anneal.

Table 7.1: Phases identified in the 1 hour/500 °C sample, their lattice parameters (and estimated standard deviation), published lattice parameters from the PDF-4+ database [149], and composition.

Phase	Param.	Value (nm)	esd (nm)	Reference[149] (nm)	Ni (at%)	Fe (at%)	Cr (at%)	Co (at%)	Mn (at%)	Zn (at%)
fcc SS	a	0.3589	0.0002		12.3	27.1	24.5	25.1	4.1	7.0
α -FeCo	a	0.2864	0.0001	0.2855	5.6	44.8	4.7	37.6	2.0	5.3
β_1 -NiZn	a	0.2775	0.0002	0.2756	46.8	3.8	2.6	3.5	5.5	37.8
	c	0.3134	0.0004	0.31927						
Cr ₂₃ C ₆	a	1.0629	0.0004	1.065	5.1	14.0	65.3	8.7	3.2	3.6

While the annealing temperatures used in this work are all below the FeCo order-disorder transition temperature, due to the highly non-equilibrium starting material and substantial amount (17.6%) of impurity atoms in the phase, we assume the FeCo is the disordered α phase. In practice, the α and α' phases are difficult to distinguish experimentally and have similar magnetic moments [152].

After the 1 hour/500 °C anneal, the lattice parameter of FeCo is larger than the reported value, which agrees with the quantitative EDS results that show an enrichment in Fe and an average of 5% Zn in the FeCo particles. The lattice parameter of Cr_{23}C_6 is slightly smaller than expected, likely due to substitution of Fe for Cr. The largest difference is seen in NiZn, which has a cell volume 0.45% smaller than the reference with the c vector having the largest difference from its expected value. EDS measurements suggest that Zn is below the stoichiometric ratio, with Mn being the largest impurity. As Zn is in the center of the cell, substituting the much smaller Mn atom would substantially decrease the cell height. As Ni is the smallest metallic element in the system, any substitutional impurities in the Ni sites would increase the a vector, as is also observed. The lattice parameter of the solid solution phase decreases by 1.1% compared to the as-milled alloy due to the loss of Zn to the NiZn phase. For reference, the close-packed atomic radii reported by Pearson [39] are also provided in Table 7.2.

Table 7.2: Close-packed atomic radii of the elements [39].

Atom	Radius (nm)
Ni	0.1246
Fe	0.1274
Cr	0.1282
Co	0.1252
Mn	0.1264
Zn	0.1394

Comparing the XRD results from 1 hour and 4 hour 500 °C treatments, the relative intensity of the peak near 44.6° increases after longer annealing times compared to the peak at 43.5°. The former corresponds to the FeCo {110} while the latter is a mixture of the fcc solid solution {111} and NiZn {101} peaks. This indicates that a larger fraction of the solution is transforming to α -FeCo given longer annealing time. The lattice parameter of the solution phase decreases only slightly however, suggesting that the NiZn precipitation occurs much faster.

After treatment temperatures at 450 °C and 600 °C, only a small amount of α -FeCo forms. After 2 hours, the lattice parameter of the solid solution phase decreases by 0.4% and 1.4% at 450 °C and 600 °C, respectively, indicating that NiZn formation is aided by higher temperatures. Carbide phases did not form at 450 °C.

Based on the Scherrer method, the grain size of the as-milled alloy is approximately 7 nm. From measurements of 25-50 grains of each phase in STEM/EDS maps of several regions, it can be seen that the material remains nanocrystalline despite the phase changes.

Grain size statistics of the precipitate phases can be seen in Table 7.3. The true average may be smaller, as extremely fine particles are difficult to distinguish from the matrix. Many of the particles are irregularly-shaped, so the horizontal and vertical axis of each particle was measured. These sizes are consistent with mechanical tests of the 2 hour/500 °C sample, which was found to have a relatively high hardness of 7.9 GPa.

Table 7.3: Grain size statistics of precipitate phases in 1 hour/500 °C sample.

Phase	Mean (nm)	Median (nm)	SD (nm)	Min (nm)	Max (nm)
FeCo	29.7	27.3	12.6	10.7	86.6
NiZn	41.8	35.6	24.4	14.4	135.1
Cr ₂₃ C ₆	28.9	25.1	10.7	15.7	65.7

The rate of NiZn precipitation appears to be related to temperature and occurs relatively quickly. FeCo precipitation however, occurs primarily within a narrow temperature window and takes several hours to approach completion, even at the optimal temperature. However, from the Fe-Co binary phase diagram [152,153], the α or α' phase should be the equilibrium phase at all temperatures used near the equiatomic composition. Unfortunately, few relevant ternary phase diagrams for this system are available. In addition, it is reasonably well established that NiFeCrCo and NiFeCrCoMn form stable fcc solid solutions [1,27,52,154]. A likely mechanism is that as NiZn forms, it removes Ni from the matrix, destabilizing the solid solution phase, allowing FeCo to form. At higher (≥ 600 °C) temperatures, however, the entropic contribution to the free energy stabilizes the solid

solution. If all the Zn forms NiZn with most of the Ni from the matrix, the remaining 5-element mixture will have a configurational entropy of $11.7 \text{ J mol}^{-1} \text{ K}^{-1}$, assuming ideal mixing. Thus, at $600 \text{ }^\circ\text{C}$, the entropy will reduce the Gibbs free energy of the mixture by 10.2 kJ mol^{-1} .

This mechanism reasonably agrees with experimental observations. At $450 \text{ }^\circ\text{C}$, only a small amount of NiZn forms and the remaining solid solution remains relatively stable. At $500\text{-}550 \text{ }^\circ\text{C}$, NiZn forms rapidly and a significant amount of FeCo forms from the solid solution. At $600 \text{ }^\circ\text{C}$, NiZn also forms rapidly, but only a small amount of FeCo forms, likely during cooling through $500 \text{ }^\circ\text{C}$. First-principles calculations of the formation energies of the phases also support this mechanism. The enthalpy of mixing of the annealed multiphase alloy is -1.04 eV/atom , lower than that of the as-milled alloy 0.00 eV/atom . The formation of the FeCo and NiZn phases is therefore energetically preferred. The enthalpy of mixing of FeCo is -0.12 eV/atom , and that of NiZn is -0.22 eV/atom , indicating a higher driving force for the formation of NiZn.

Additionally, the milled alloy is nanocrystalline with an extremely small grain size and high defect density. This creates a non-equilibrium condition with high strain and interfacial energy with many triple junctions, grain boundaries, and dislocations that can serve as nucleation sites for precipitates.

7.4.2. Magnetic properties

The as-milled material is paramagnetic at room temperature and ferromagnetic at cryogenic temperatures, similar to the base NiFeCrCo alloy, and exhibiting a similar gradual transition from the FM to PM state [52]. However, its saturation magnetization at 1.8 K is lower, 27 emu/g compared to >50 emu/g for ball-milled NiFeCrCo. This is likely due to the reduced amount of ferromagnetic elements and addition of antiferromagnetic Mn.

Figure 7.3 shows a representative 300K M vs. H curve for the alloy after the 1 hour/500°C annealing treatment. Figure 7.4 shows the saturation magnetization (M_s), remanence (M_r), intrinsic coercivity (H_{ci}), and maximum energy product (BH_{max}) of the alloy as a function of annealing temperature and time. The hard magnetic properties are optimized near 1 hour at 500 °C, while M_s continues to increase with longer annealing times. This supports the conclusions of the microstructure analysis, that the FeCo phase continues to form from the paramagnetic fcc matrix with extended annealing times.

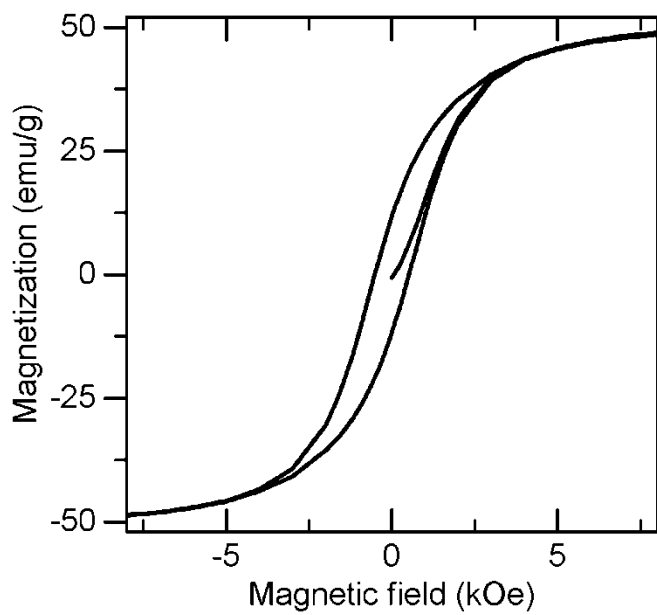
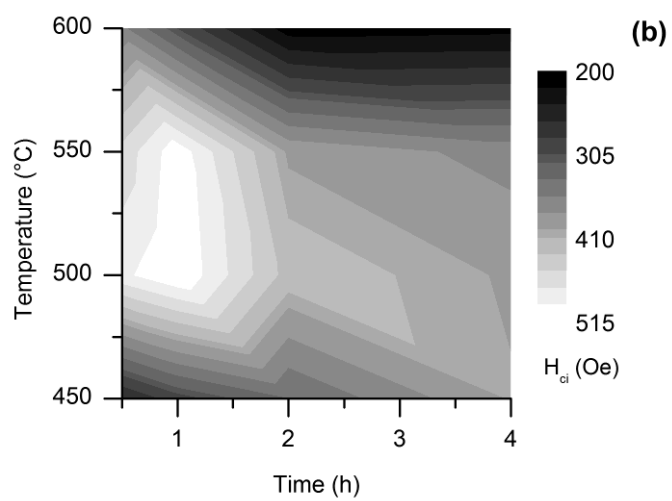
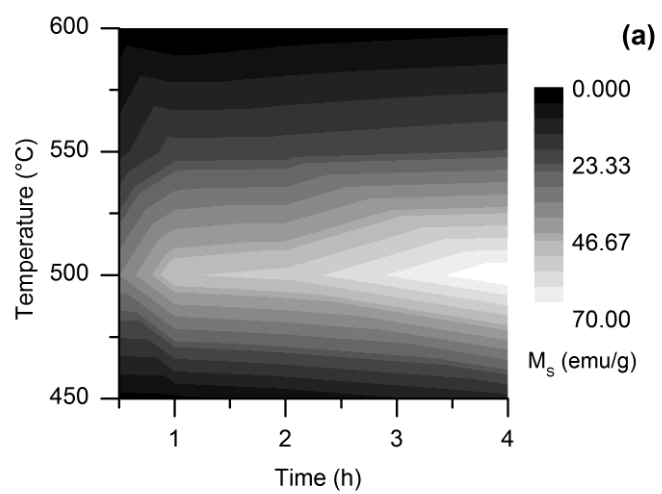
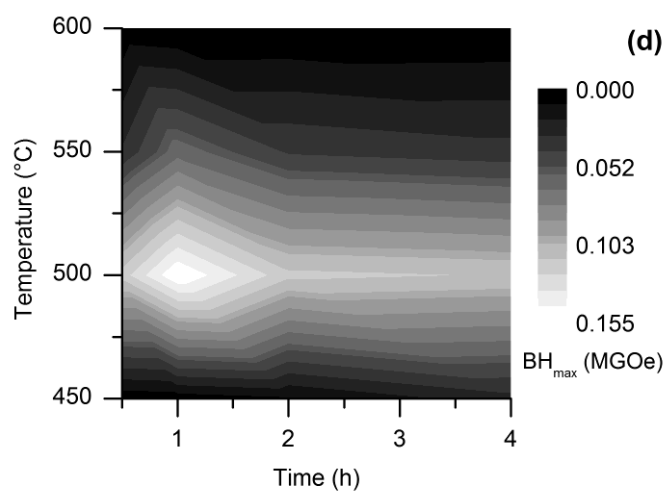
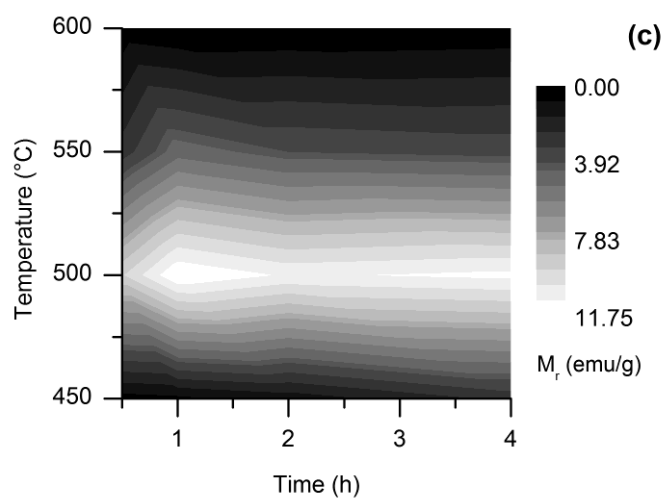


Figure 7.3: Magnetization vs. field curve for 1 hour/500 °C sample

Figure 7.4: Magnetic properties as a function of annealing temperature and time. a) Saturation magnetization, b) intrinsic coercivity, c) remanence, and d) maximum energy product.





After annealing at 450 °C or 600 °C, the alloy is almost entirely paramagnetic at room temperature, though a small hysteresis loop is still present. Coercivity is least affected by temperature, with little difference between the 500 °C and 550 °C treatments at each time increment and relatively high values after 450 °C treatments.

As other multiphase metallic alloys are improved by thermomagnetic treatments [155,156], a single sample was annealed for 1 hour at 500 °C in a 3 T magnetic field. There was no significant difference in coercivity or remanence compared to the sample annealed at the same temperature and time without a field. Saturation magnetization was slightly smaller, likely explained by differences in heating and cooling rates between the two furnaces. This is likely due to the lower Co content than commercial Alnico alloys, in which at least 24% Co is necessary for thermomagnetic treatments to be effective [157].

Since the FeCo grains are small (<50 nm), irregularly shaped, and generally isolated from each other within the matrix and other phases, they may be acting as single-domain particles, which would result in increased coercive force. This is supported by the reduction in coercivity with longer annealing times. While the amount of FeCo increases, increasing M_s , this likely occurs by coarsening rather than additional precipitation, increasing the particle size above the single-domain threshold. First-principles modeling by Burkert et al. predicted that certain tetragonally-distorted FeCo structures have extremely high magnetic anisotropy [158], but there was no significant distortion observed in this material despite the impurity content.

First principles modeling was also used in this study to calculate the magnetic moment of the alloy at 0 K. This was compared to magnetization measurements at 1.8 K. A random solid solution (RSS) was used to simulate the as-milled alloy. This RSS has a predicted moment of $0.43 \mu_B/\text{atom}$. To simulate the experimentally annealed material, we make the assumption that three phases are present. The first contains Fe and Co and forms as a RSS on the bcc lattice. The second contains Ni and Zn, which forms an ordered $L1_0$ alloy. The third contains the remaining elements as a RSS on the fcc lattice with composition of $\text{Cr}_{61.1}\text{Mn}_{12.3}\text{Fe}_{13.8}\text{Ni}_{12.9}$. The total magnetic moment for the annealed material is then weighted by molar fraction based on total alloy composition and is predicted to be $0.82 \mu_B/\text{atom}$. The spontaneous magnetization was determined from the 1.8 K magnetization vs. field curves by extrapolating the saturation region to zero field using a linear fit. The spontaneous magnetization of the as-milled alloy is 22.6 emu/g , and that of the 1 hour/ 500°C sample is 50.6 emu/g . This is a 124% relative increase in the magnetic moment, which is a slightly higher percent increase when compared with the computationally predicted 91% increase of the magnetic moment. This disagreement may be due, in part, to a number of factors. First, the annealed alloy is simulated with three phases in isolation and no collective magnetic interactions between the phases are accounted for in the simulations. Second, as has been shown for similar complex solid solution alloys, the magnetic moment can vary by large amounts as a result of relatively small amounts of short-range atomic ordering [52], making prediction difficult. The possibility of short range chemical ordering in the simulated as-milled alloy was not considered. Including this effect may reduce the moment of the as-

milled material and improve the percent increase. Regardless, the simulation results agree with the experimental trend that phase separation supports a significant increase in the bulk magnetic moment.

Compared to the few published HEA-based permanent magnets, NiFeCrCoZnMn performs well. The coercivity is nearly double that of AlCoCrCuFeNi and the remanence ratio (M_r/M_s) is nearly tripled. The coercivity reported here is lower than that of BiFeCoNiMn, but NiFeCrCoZnMn can be produced in bulk forms.

The results presented in this work represent the first attempt at producing a NiFeCrCoZnMn alloy. Future work will likely be able to obtain better results through optimization of the composition and processing. Better properties may be achievable by further reducing the stability of the matrix phase relative to FeCo, increasing the driving force for precipitation. In this work, the effect of the $Cr_{23}C_6$ particles was not considered; future research may examine their influence on the microstructure and magnetic properties. They have the smallest particle size of the precipitate phases so they may serve to stabilize the nanocrystalline grain size via Zener pinning.

7.5. Conclusion

A hard magnetic NiFeCrCoZnMn alloy was produced using mechanical alloying and annealing. The alloy was designed using high-entropy alloy principles, but the solid solution phase formed during milling was found to be unstable at elevated temperatures.

XRD, STEM/EDS, and first-principles modeling was used to characterize the microstructure and determine the likely phase transformation mechanisms. Despite the relatively small $|\Delta H_{mix}|$ of the Ni-Zn binary and the small average atomic size difference of the alloy, NiZn formation is energetically favorable compared to the high-entropy solid solution. As NiZn forms, the stability of the solid solution matrix decreases, allowing the magnetic phase, α -FeCo to form. However, while NiZn formation is aided by higher temperatures, α -FeCo formation decreases as the temperature is increased above 500 °C. This was attributed to the high configurational entropy of the matrix phase, which decreases the Gibbs free energy of the solution significantly at high temperatures. Cr_{23}C_6 also formed, but its influence was not studied.

Despite being substantially similar to previously developed high-entropy alloys, the behavior of the alloy disagreed with the empirical models commonly used to develop HEAs. This illustrates the need for more robust alloy development guidelines for multi-principal element alloys.

After optimal processing conditions, the alloy has a 300 K intrinsic coercivity of 515 Oe, saturation magnetization of 50 emu/g, and maximum energy product of 0.155 MGOe. While this is not competitive with current generations of commercial magnets, it compares favorably to other HEA-based magnets and optimization of the composition will likely be able to improve these properties. Additionally, this system may offer other benefits, such as its high mechanical hardness, simple processing technique, and rare earth-free composition.

8. CONCLUSIONS

The physical properties of a series of NiFeCrCo-based alloys have been investigated using a variety of microstructural and mechanical characterization methods. The stacking fault energy of the equiatomic NiFeCrCoMn alloy was found to be 18 – 27 mJ m⁻² using both a combination of experimental and computational values. This range is consistent with the mechanical properties and deformation mechanisms of the alloy. The SFE can be tailored using relatively small changes to the composition, by changing the ratio of Ni to Cr or varying the Co content.

However, despite the lower SFE of some of the non-equiatomic NiFeCrCoMn alloys, equiatomic NiFeCrCo had a better combination of strength and ductility, giving it a higher toughness than any of the 5-component alloys. This was attributed to the presence of Mn oxides in the 5-component alloys. The alloys also have a high strain-hardening rate, contributing to their high toughness, and the strain-hardening behavior was found to be grain size dependent. While alloys with low Ni and high Cr content form solid solutions when cast and homogenized, they tend to form σ -phase intermetallics when annealed at moderate temperatures following cold rolling, which is highly deleterious to ductility.

The single crystal elastic constants of equiatomic NiFeCrCoMn were measured using nanoindentation of individual grains in a polycrystalline sample. $C_{11} = 215$ GPa, $C_{12} = 107$ GPa, and $C_{44} = 103$ GPa. These measured values are consistent with those calculated using first-principles modeling. The stacking fault energy measured using these values also falls within the range estimated using the calculated elastic constants.

As a result of adding Zn to the base 5-component alloy, and reducing the amount of Mn, the alloy no longer forms a stable solid solution. Mechanical alloying can produce a metastable solid solution, but annealing causes the alloy to form several other phases. NiZn forms, further reducing the stability of the solution, allowing FeCo to form. FeCo precipitates as nano-sized particles, resulting in a material ferromagnetic at room temperature. At the optimal annealing temperature, the material has an intrinsic coercivity of 515 Oe and saturation magnetization of 50 emu/g. Longer heat treatments can increase the saturation, but result in lower coercivity.

There are still numerous opportunities for further research on this topic. This work essentially represents only an initial investigation into the basic physical properties of a small fraction of the NiFeCrCo alloy system. The stacking fault energies measured here should be verified by direct electron microscopy measurements. Additionally, the stacking fault energy should be measured as a function of temperature and with other non-equiatomic compositions. In this work, mechanical testing was only done using conventionally processed materials. High-pressure torsion or equal-channel angular extrusion could be used to produce ultrafine-grained material to determine whether the high ductility and strain-hardening still exists at extremely small grain sizes. The elastic constants measured here should be verified using conventional measurements on a single-crystal sample. The elastic constants also remain unmeasured in NiFeCrCo and non-equiatomic alloys. The magnetic properties of NiFeCrCoMnZn could likely be improved by optimizing the composition in addition to the processing parameters. Increasing the driving force for FeCo formation would likely improve

the magnetic properties. Finally, the properties measured here may be useful to measure other mechanical properties, as well as evaluate NiFeCrCo alloys for potential processing methods and applications.

REFERENCES

- [1] B. Cantor, I.T.H. Chang, P. Knight, A.J.B. Vincent, *Mater. Sci. Eng. A* 375-377 (2004) 213.
- [2] J.W. Yeh, S.K. Chen, S.J. Lin, J.Y. Gan, T.S. Chin, T.T. Shun, C.H. Tsau, S.Y. Chang, *Adv. Eng. Mater.* 6 (2004) 299.
- [3] Y. Zhang, T.T. Zuo, Z. Tang, M.C. Gao, K.A. Dahmen, P.K. Liaw, Z.P. Lu, *Prog. Mater. Sci.* 61 (2014) 1.
- [4] Z. Wu, H. Bei, G.M. Pharr, E.P. George, *Acta Mater.* 81 (2014) 428.
- [5] A.F. Giamei, D.L. Anton, *Metall. Trans. A* 16 (1985) 1997.
- [6] L. Li, W. Xu, M. Saber, Y. Zhu, C.C. Koch, R.O. Scattergood, *Mater. Sci. Eng. A* 636 (2015) 565.
- [7] O.N. Senkov, G.B. Wilks, J.M. Scott, D.B. Miracle, *Intermetallics* 19 (2011) 698.
- [8] A. Takeuchi, K. Amiya, T. Wada, K. Yubuta, W. Zhang, *JOM* 66 (2014) 1984.
- [9] K.M. Youssef, A.J. Zaddach, C. Niu, D.L. Irving, C.C. Koch, *Mater. Res. Lett.* (2014) 1.
- [10] M. Feuerbacher, M. Heidelmann, C. Thomas, *Mater. Res. Lett.* 3 (2014) 1.

- [11] S.C. Middleburgh, D.M. King, G.R. Lumpkin, *R. Soc. Open Sci.* 2 (2015) 140292.
- [12] Y. Zou, S. Maiti, W. Steurer, R. Spolenak, *Acta Mater.* 65 (2014) 85.
- [13] F. Otto, A. Dlouhý, C. Somsen, H. Bei, G. Eggeler, E.P. George, *Acta Mater.* 61 (2013) 5743.
- [14] C. Tung, J. Yeh, T. Shun, S. Chen, Y. Huang, H. Chen, *Mater. Lett.* 61 (2007) 1.
- [15] S. Varalakshmi, M. Kamaraj, B.S. Murty, *J. Alloys Compd.* 460 (2008) 253.
- [16] Y.-L. Chen, Y.-H. Hu, C.-A. Hsieh, J.-W. Yeh, S.-K. Chen, *J. Alloys Compd.* 481 (2009) 768.
- [17] K.B. Zhang, Z.Y. Fu, J.Y. Zhang, W.M. Wang, S.W. Lee, K. Niihara, *J. Alloys Compd.* 495 (2010) 33.
- [18] A.J. Zaddach, C. Niu, C.C. Koch, D.L. Irving, *JOM* 65 (2013) 1780.
- [19] L.M. Wang, C.C. Chen, J.W. Yeh, S.T. Ke, *Mater. Chem. Phys.* 126 (2011) 880.
- [20] H. Zhang, Y. Pan, Y. He, *J. Therm. Spray Technol.* 20 (2011) 1049.
- [21] V. Dolique, A.-L. Thomann, P. Brault, *IEEE Trans. Plasma Sci.* 39 (2011) 2478.
- [22] C.-Z. Yao, P. Zhang, M. Liu, G.-R. Li, J.-Q. Ye, P. Liu, Y.-X. Tong, *Electrochim. Acta* 53 (2008) 8359.

- [23] U.S. Hsu, U.D. Hung, J.W. Yeh, S.K. Chen, Y.S. Huang, C.C. Yang, *Mater. Sci. Eng. A* 461 (2007) 403.
- [24] a. Gali, E.P. George, *Intermetallics* 39 (2013) 74.
- [25] J.W. Yeh, Y.L. Chen, S.J. Lin, S.K. Chen, in: *Mater. Sci. Forum*, 2007, pp. 1–9.
- [26] E.-W. Huang, D. Yu, J.-W. Yeh, C. Lee, K. An, S.-Y. Tu, *Scr. Mater.* 101 (2015) 32.
- [27] F. Otto, Y. Yang, H. Bei, E.P. George, *Acta Mater.* 61 (2013) 2628.
- [28] T.-T. Shun, Y.-C. Du, *J. Alloys Compd.* 478 (2009) 269.
- [29] Y. Zhang, X. Yang, P.K. Liaw, *Jom* 64 (2012) 830.
- [30] A.L. Greer, *Nature* 366 (1993) 303.
- [31] W.A. Oates, *J. Phase Equilibria Diffus.* 28 (2007) 79.
- [32] S.Q. Wang, *Mater. Sci. Forum* 749 (2013) 479.
- [33] A. Takeuchi, A. Inoue, *Mater. Trans.* 46 (2005) 2817.
- [34] A.R. Miedema, F.R. de Boer, R. Boom, *Calphad* 1 (1977) 341.
- [35] A.K. Niessen, F.R. de Boer, R. Boom, P.F. de Châtel, W.C.M. Mattens, A.R. Miedema, *Calphad* 7 (1983) 51.

- [36] Y. Zhang, Y. Zhou, J. Lin, *Adv. Eng. Mater.* 10 (2008) 534.
- [37] O.N. Senkov, J.D. Miller, D.B. Miracle, C. Woodward, *Calphad* 50 (2015) 32.
- [38] F. Zhang, C. Zhang, S.L. Chen, J. Zhu, W.S. Cao, U.R. Kattner, *Calphad* 45 (2014) 1.
- [39] W.B. Pearson, *The Crystal Chemistry and Physics of Metals and Alloys*, John Wiley and Sons, New York, 1972.
- [40] L. Pauling, *J. Am. Chem. Soc.* 69 (1947) 542.
- [41] G.P. Tiwari, R. V. Ramanujan, *J. Mater. Sci.* 36 271.
- [42] S. Guo, C. Ng, J. Lu, C. Liu, *J. Appl. Phys.* 109 (2011) 103505.
- [43] M.-H. Tsai, K.-Y. Tsai, C.-W. Tsai, C. Lee, C.-C. Juan, J.-W. Yeh, *Mater. Res. Lett.* 1 (2013) 207.
- [44] T.-T. Shun, L.-Y. Chang, M.-H. Shiu, *Mater. Sci. Eng. A* 556 (2012) 170.
- [45] T.-T. Shun, L.-Y. Chang, M.-H. Shiu, *Mater. Charact.* 70 (2012) 63.
- [46] S.G. Ma, S.F. Zhang, M.C. Gao, P.K. Liaw, Y. Zhang, *JOM* 65 (2013) 1751.
- [47] B. Gludovatz, A. Hohenwarter, D. Catoor, E.H. Chang, E.P. George, R.O. Ritchie, *Science* 345 (2014) 1153.

- [48] A. Haglund, M. Koehler, D. Catoor, E.P. George, V. Keppens, *Intermetallics* 58 (2015) 62.
- [49] C. Zhu, Z.P. Lu, T.G. Nieh, *Acta Mater.* (2013) 1.
- [50] P.P. Bhattacharjee, G.D. Sathiaraj, M. Zaid, J.R. Gatti, C. Lee, C.-W. Tsai, J.-W. Yeh, *J. Alloys Compd.* 587 (2014) 544.
- [51] K.-Y. Tsai, M.-H. Tsai, J.-W. Yeh, *Acta Mater.* null (2013).
- [52] C. Niu, A.J. Zaddach, A.A. Oni, X. Sang, J.W.H. III, J.M. LeBeau, C.C. Koch, D.L. Irving, *Appl. Phys. Lett.* 106 (2015) 161906.
- [53] N. Hansen, *Scr. Mater.* 51 (2004) 801.
- [54] G.E. Dieter, *Mechanical Metallurgy*, McGraw-Hill, New York, 1986.
- [55] C.E. Carlton, P.J. Ferreira, *Acta Mater.* 55 (2007) 3749.
- [56] W.F. Hosford, *Mechanical Behavior of Materials*, Cambridge University Press, 2010.
- [57] Y.L. Gong, C.E. Wen, Y.C. Li, X.X. Wu, L.P. Cheng, X.C. Han, X.K. Zhu, *Mater. Sci. Eng. A* 569 (2013) 144.
- [58] P.-L. Sun, Y.H. Zhao, J.C. Cooley, M.E. Kassner, Z. Horita, T.G. Langdon, E.J. Lavernia, Y.T. Zhu, *Mater. Sci. Eng. A* 525 (2009) 83.

- [59] D.T. Pierce, J. Bentley, J. a. Jiménez, J.E. Wittig, *Scr. Mater.* 66 (2012) 753.
- [60] D.T. Pierce, K. Nowag, A. Montagne, J.A. Jiménez, J.E. Wittig, R. Ghisleni, *Mater. Sci. Eng. A* 578 (2013) 134.
- [61] Y.H. Zhao, Y.T. Zhu, X.Z. Liao, Z. Horita, T.G. Langdon, *Appl. Phys. Lett.* 89 (2006) 121906.
- [62] S. Takeuchi, *J. Phys. Soc. Japan* 27 (1969) 929.
- [63] Z. Yang, M.F. Chisholm, G. Duscher, X. Ma, S.J. Pennycook, *Acta Mater.* 61 (2013) 350.
- [64] C. Suryanarayana, *Prog. Mater. Sci.* 46 (2001) 1.
- [65] S. Arajs, G. Wray, *J. Phys. E.* 518 (1969).
- [66] R.D. Doherty, D.A. Hughes, F.J. Humphreys, J.J. Jonas, D.J. Jensen, M.E. Kassner, W.E. King, T.R. McNelley, H.J. McQueen, A.D. Rollett, *Mater. Sci. Eng. A* 238 (1997) 219.
- [67] W.D. Callister, D.G. Rethwisch, *Fundamentals of Materials Science and Engineering: An Integrated Approach*, 3rd ed., John Wiley and Sons, Hoboken, 2008.
- [68] W.C. Oliver, G.M. Pharr, *J. Mater. Res.* 7 (1992) 1564.

- [69] G. Caglioti, A. Paoletti, F.P. Ricci, Nucl. Instruments 3 (1958) 223.
- [70] B.D. Cullity, S.R. Stock, Elements of X-Ray Diffraction, 3rd ed., Prentice-Hall, Upper Saddle River, NJ, 2001.
- [71] G. Williamson, W. Hall, Acta Metall. 1 (1953) 22.
- [72] M. Leoni, T. Confente, P. Scardi, Zeitschrift Für Krist. Suppl. 2006 (2006) 249.
- [73] R. Schramm, R. Reed, Metall. Trans. A 7 (1976) 359.
- [74] H. Klug, L. Alexander, X-Ray Diffraction Procedures: For Polycrystalline and Amorphous Materials, Wiley-Interscience, New York, 1974.
- [75] E407-07e1: Standard Practice for Microetching Metals and Alloys, ASTM International, West Conshohocken, PA, 2011.
- [76] J. Goldstein, D. Newbury, D. Joy, C. Lyman, P. Echlin, E. Lifshin, L. Sawyer, J. Michael, Scanning Electron Microscopy and X-Ray Microanalysis, 3rd ed., Springer, New York, 2003.
- [77] T. Tao, J. Vac. Sci. Technol. B Microelectron. Nanom. Struct. 8 (1990) 1826.
- [78] W.Y. Kwong, W.Y. Zhang, in: ISSM 2005, IEEE Int. Symp. Semicond. Manuf. 2005., IEEE, 2005, pp. 469–471.

- [79] L.A. Giannuzzi, J.L. Drown, S.R. Brown, R.B. Irwin, F.A. Stevie, *Microsc. Res. Tech.* 41 (1998) 285.
- [80] K. Youssef, M. Sakaliyska, H. Bahmanpour, R. Scattergood, C. Koch, *Acta Mater.* 59 (2011) 5758.
- [81] H. Bahmanpour, A. Kauffmann, M.S. Khoshkhoo, K.M. Youssef, S. Mula, J. Freudenberger, J. Eckert, R.O. Scattergood, C.C. Koch, *Mater. Sci. Eng. A* 529 (2011) 230.
- [82] Z.W. Wang, Y.B. Wang, X.Z. Liao, Y.H. Zhao, E.J. Lavernia, Y.T. Zhu, Z. Horita, T.G. Langdon, *Scr. Mater.* 60 (2009) 52.
- [83] X.H. An, Q.Y. Lin, S.D. Wu, Z.F. Zhang, R.B. Figueiredo, N. Gao, T.G. Langdon, *Scr. Mater.* 64 (2011) 954.
- [84] Y. Zhang, N.R. Tao, K. Lu, *Scr. Mater.* 60 (2009) 211.
- [85] W.W. Jian, G.M. Cheng, W.Z. Xu, H. Yuan, M.H. Tsai, Q.D. Wang, C.C. Koch, Y.T. Zhu, S.N. Mathaudhu, *Mater. Res. Lett.* 1 (2013) 61.
- [86] S. Guo, C.T. Liu, *Prog. Nat. Sci. Mater. Int.* 21 (2011) 433.
- [87] R.J.D. Tilley, *Understanding Solids: The Science of Materials*, Wiley, Hoboken, 2004.
- [88] L. Vitos, *Phys. Rev. B* 64 (2001) 014107.

- [89] L. Vitos, *Computational Quantum Mechanics for Materials Engineers: The EMTO Method and Applications*, Springer-Verlag, London, 2007.
- [90] P. Soven, *Phys. Rev.* 156 (1967) 809.
- [91] L. Vitos, I.A. Abrikosov, B. Johansson, *Phys. Rev. Lett.* 87 (2001) 156401.
- [92] G. Kresse, J. Hafner, *Phys. Rev. B* 47 (1993) 558.
- [93] G. Kresse, *Phys. Rev. B* 54 (1996) 11169.
- [94] G. Kresse, J. Furthmüller, *Comput. Mater. Sci.* 6 (1996) 15.
- [95] G. Kresse, J. Hafner, *Phys. Rev. B* 49 (1994) 14251.
- [96] A. Zunger, S.-H. Wei, L.G. Ferreira, J.E. Bernard, *Phys. Rev. Lett.* 65 (1990) 353.
- [97] A. van de Walle, M. Asta, G. Ceder, *Calphad* 26 (2002) 539.
- [98] O. Andersen, O. Jepsen, G. Krier, *Lectures on Methods of Electronic Structure Calculations*, World Scientific, Singapore, 1994.
- [99] L. Vitos, P.A. Korzhavyi, B. Johansson, *Phys. Rev. Lett.* 88 (2002) 155501.
- [100] L. Vitos, P.A. Korzhavyi, J.-O. Nilsson, B. Johansson, *Phys. Scr.* 77 (2008) 065703.
- [101] J.P. Perdew, K. Burke, M. Ernzerhof, *Phys. Rev. Lett.* 78 (1997) 1396.

- [102] J.P. Perdew, K. Burke, M. Ernzerhof, *Phys. Rev. Lett.* 77 (1996) 3865.
- [103] B.L. Gyorffy, A.J. Pindor, J. Staunton, G.M. Stocks, H. Winter, *J. Phys. F Met. Phys.* 15 (1985) 1337.
- [104] P.E. Blöchl, *Phys. Rev. B* 50 (1994) 17953.
- [105] G. Kresse, *Phys. Rev. B* 59 (1999) 1758.
- [106] C. Jiang, L.-Q. Chen, Z.-K. Liu, *Acta Mater.* 53 (2005) 2643.
- [107] J. von Pezold, A. Dick, M. Friák, J. Neugebauer, *Phys. Rev. B* 81 (2010) 094203.
- [108] S. Lu, Q.-M. Hu, E.K. Delczeg-Czirjak, B. Johansson, L. Vitos, *Acta Mater.* 60 (2012) 4506.
- [109] L. Vitos, J.-O. Nilsson, B. Johansson, *Acta Mater.* 54 (2006) 3821.
- [110] M.S. Lucas, L. Mauger, J.A. Muñoz, Y. Xiao, A.O. Sheets, S.L. Semiatin, J. Horwath, Z. Turgut, *J. Appl. Phys.* 109 (2011) 07E307.
- [111] S. Vives, E. Gaffet, C. Meunier, *Mater. Sci. Eng. A* 366 (2004) 229.
- [112] M.J. Mehl, J.E. Osburn, D.A. Papaconstantopoulos, B.M. Klein, *Phys. Rev. B* 41 (1990) 10311.
- [113] F. Tian, L.K. Varga, N. Chen, L. Delczeg, L. Vitos, *Phys. Rev. B* 87 (2013) 075144.

- [114] G. Grimvall, *Thermophysical Properties of Materials*, North-Holland, Amsterdam, 1999.
- [115] H. Ledbetter, R. Reed, *J. Phys. Chem. Ref. Data* 2 (1973) 531.
- [116] R. Schramm, R. Reed, *Metall. Trans. A* 6 (1975).
- [117] C.B. Carter, S.M. Holmes, *Philos. Mag.* 35 (2006) 1161.
- [118] M.F. Denanot, J.P. Villain, *Phys. Status Solidi* 8 (1971) K125.
- [119] S. Mohanty, N.P. Gurao, K. Biswas, *Mater. Sci. Eng. A* 617 (2014) 211.
- [120] M.J. Yao, K.G. Pradeep, C.C. Tasan, D. Raabe, *Scr. Mater.* 72-73 (2014) 5.
- [121] V.S. Sarma, J. Wang, W.W. Jian, A. Kauffmann, H. Conrad, J. Freudenberger, Y.T. Zhu, *Mater. Sci. Eng. A* 527 (2010) 7624.
- [122] I. Gutierrez-Urrutia, D. Raabe, *Scr. Mater.* 66 (2012) 992.
- [123] A.J. Zaddach, C. Niu, K.M. Youssef, D.L. Irving, C. Koch, in: *TMS 2014*, San Diego, CA, 2014.
- [124] Y. Zhang, Y.J. Zhou, *Mater. Sci. Forum* 561-565 (2007) 1337.
- [125] C.A. Schneider, W.S. Rasband, K.W. Eliceiri, *Nat. Methods* 9 (2012) 671.

- [126] M.-H. Tsai, K.-Y. Tsai, C.-W. Tsai, C. Lee, C.-C. Juan, J.-W. Yeh, *Mater. Res. Lett.* 1 (2013) 207.
- [127] S. Curtze, V.-T. Kuokkala, *Acta Mater.* 58 (2010) 5129.
- [128] Rigidity Modulus: Periodicity, WebElements, Retrieved from:
http://www.webelements.com/periodicity/rigidity_modulus/.
- [129] D. Broek, *Eng. Fract. Mech.* 5 (1973) 55.
- [130] R.H. Van Stone, T.B. Cox, J.R.L. Jr., J.A. Psioda, (2013).
- [131] H. Paul, J. Driver, C. Maurice, A. Piatkowski, *Acta Mater.* 55 (2007) 575.
- [132] D. Raabe, M. Sachtleber, H. Weiland, G. Scheele, Z. Zhao, *Acta Mater.* 51 (2003) 1539.
- [133] N. Stepanov, M. Tikhonovsky, N. Yurchenko, D. Zyabkin, M. Klimova, S. Zherebtsov, A. Efimov, G. Salishchev, *Intermetallics* 59 (2015) 8.
- [134] I. Toda-Caraballo, P.E.J. Rivera-Díaz-del-Castillo, *Acta Mater.* 85 (2015) 14.
- [135] S. Varalakshmi, M. Kamaraj, B.S. Murty, *Mater. Sci. Eng. A* 527 (2010) 1027.
- [136] E. Aerts, P. Delavignette, R. Siems, S. Amelinckx, *J. Appl. Phys.* 33 (1962) 3078.
- [137] R. Yu, J. Zhu, H.Q. Ye, *Comput. Phys. Commun.* 181 (2010) 671.

- [138] L. Cain, J. Thomas, *Phys. Rev. B* (1971).
- [139] U. Bayerlein, H.G. Sockel, in: *Superalloys 1992*, 1992, pp. 695–704.
- [140] O.L. Anderson, *J. Phys. Chem. Solids* 24 (1963) 909.
- [141] H.M. Ledbetter, *Phys. Status Solidi* 85 (1984) 89.
- [142] J.J. Vlassak, W.D. Nix, *J. Mech. Phys. Solids* 42 (1994) 1223.
- [143] E. Jones, T. Oliphant, P. Peterson, *SciPy: Open Source Scientific Tools for Python*, 2001, Retrieved from: <http://www.scipy.org/>.
- [144] C.A. Julien, F.G. Jones, *J. Appl. Phys.* 36 (1965) 1173.
- [145] M. Sundararaman, P. Mukhopadhyay, S. Banerjee, *Metall. Trans. A* 23 (1992) 2015.
- [146] T.-T. Shun, C.-H. Hung, C.-F. Lee, *J. Alloys Compd.* 495 (2010) 55.
- [147] C.-Y. Hsu, J.-W. Yeh, S.-K. Chen, T.-T. Shun, *Metall. Mater. Trans. A* 35 (2004) 1465.
- [148] S. Singh, N. Wanderka, K. Kiefer, K. Siemensmeyer, J. Banhart, *Ultramicroscopy* 111 (2011) 619.
- [149] ICDD, PDF-4+ 2010 (Database), International Centre for Diffraction Data, Newtown Square, PA, 2010.

- [150] M. Hebbache, M. Zenzemi, *Phys. Rev. B* 70 (2004) 224107.
- [151] X. Yang, Y. Zhang, *Mater. Chem. Phys.* 132 (2012) 233.
- [152] I. Ohnuma, H. Enoki, O. Ikeda, R. Kainuma, H. Ohtani, B. Sundman, K. Ishida, *Acta Mater.* 50 (2002) 379.
- [153] H. Okamoto, *J. Phase Equilibria Diffus.* 29 (2008) 383.
- [154] S.C. Middleburgh, D.M. King, G.R. Lumpkin, M. Cortie, L. Edwards, *J. Alloys Compd.* (2014).
- [155] S. Sugimoto, J. Honda, Y. Ohtani, M. Okada, M. Homma, *IEEE Trans. Magn.* 23 (1987) 3193.
- [156] E.G. Povolotskii, Y.M. Dovgalevskii, V.K. Baitina, *Met. Sci. Heat Treat.* 5 (1963) 631.
- [157] M. Stanek, L. Wierzbicki, M. Leonowicz, *Arch. Metall. Mater.* 55 (2010) 571.
- [158] T. Burkert, L. Nordström, O. Eriksson, O. Heinonen, *Phys. Rev. Lett.* 93 (2004) 027203.

APPENDIX

Code for calculation of elastic constants using nanoindentation data

```

#!/usr/bin/python
from scipy import optimize
import sys

M111 = M100 = E = v = G = 0

# HKE method
def HKE_method(c11, c12, c44):
    alpha = (5.0*c11 + 4.0*c12)/(8.0)
    beta = -1.0*(c44*(7.0*c11 - 4.0*c12))/(8.0)
    gamma = -1.0*(c44*(c11 - c12)*(c11 + 2.0*c12))/(8.0)
    return (G**3.0 + alpha*G**2.0 + beta*G + gamma)

# Vlassak-Nix model
def VN_model(c11, c12, c44):
    return M111/M100 - beta_111(c11, c12, c44)/beta_100(c11, c12, c44)

# Beta_100 in VN-model, constants extrapolated using 5th order polynomials
def beta_100(c11, c12, c44):
    v100 = c12/(c11 + c12)
    a = fifth_order(-1.35199999998819, 52.1683333331464, -368.883333332168,
                    1241.33333332976, -2046.66666666127, 1333.33333333012, v100)
    c = fifth_order(3.1919999999665, -66.094999999422, 458.983333332945,
                    -1525.9999999872, 2486.66666666461, -1599.9999999869, v100)
    A0 = 0
    B = fifth_order(3.21399999998839, -52.7718999998155, 363.288333332182,
                    -1222.66666666313, 2036.66666666133, -1349.33333333016, v100)
    return a + c*(anis_ratio(c11, c12, c44) - A0)**B

# Beta_111 in VN-model, constants extrapolated using 5th order polynomials
def beta_111(c11, c12, c44):
    v100 = c12/(c11 + c12)
    a = fifth_order(0.921000000005946, 9.16599999990606, -137.133333332749,
                    670.999999998216, -1386.66666666398, 1039.99999999841, v100)
    c = fifth_order(1.0759999999076, -25.5336666665205, 245.283333332423,
                    -1026.9999999721, 1966.66666666247, -1413.33333333084, v100)
    A0 = fifth_order(35.695999999709, -602.169333332831, 4031.86666666329,
                    -13333.3333333222, 21733.3333333154, -13973.3333333219, v100)
    B = fifth_order(-1.5555999998924, 38.3363999998294, -308.08333333227,
                    1165.39999999674, -2102.66666666175, 1455.99999999707, v100)
    return a + c*(anis_ratio(c11, c12, c44) - A0)**B

# Fifth-order polynomial
def fifth_order(I, B1, B2, B3, B4, B5, x):
    return I + B1*x + B2*x**2 + B3*x**3 + B4*x**4 + B5*x**5

# Elastic anisotropy ratio
def anis_ratio(c11, c12, c44):
    return (2.0*c44)/(c11 - c12)

# Assume polycrystalline and single crystal bulk moduli are equal
def bulk_modulus(c11, c12):
    return E/(3.0*(1.0 - 2.0*v)) - (c11 + 2.0*c12)/(3.0)

def equations(params):

```

```

    c11, c12, c44 = params
    return (HKE_method(c11, c12, c44),
            VN_model(c11, c12, c44),
            bulk_modulus(c11, c12)
    )

if __name__ == '__main__':
    if len(sys.argv) == 5 or len(sys.argv) == 8:
        M100 = float(sys.argv[1])
        M111 = float(sys.argv[2])
        E = float(sys.argv[3])
        v = float(sys.argv[4])
        G = E/(2.0*(v + 1.0))
        if len(sys.argv) == 8:
            initial = (float(sys.argv[5]), float(sys.argv[6]), float(sys.argv[7]))
        else:
            initial = (150, 50, 100)
        # Solve using Levenberg-Marquardt non-linear least squares method
        res = optimize.root(equations, initial,
                            method='lm', options = {'maxiter':500000})
        vals = [round(x, 2) for x in res.x]
        print("c11 = {0[0]}\nc12 = {0[1]}\nc44 = {0[2]}".format(vals))
        print("\nIterations: {0}\n".format(res.nfev))
        print("""Equation results (should be zero!):
HKE method: {0[0]}
VN model: {0[1]}
Bulk modulus relation: {0[2]}""".format([round(x, 8) for x in equations(res.x)]))
    )
    else:
        print("""Invalid options.
Usage:
python elastic.py M100 M111 E v [c11 c12 c44]
M100 / M111 - Indentation moduli
E - Young's modulus
v - Poisson's ratio
c11 c12 c44 - initial guesses for elastic constants (optional)
default intitial guess: (150, 50, 100)""")
    )

```